AGU100 ADVANCING EARTH AND SPACE SCIENCE

JGR

Journal of Geophysical Research: Atmospheres

RESEARCH ARTICLE

10.1029/2018JD029011

Key Points:
- MODIS-derived SWIR corresponded better with EF than those without using SWIR
- MODIS-derived SWIRs were used as proxies for water supply to estimate LE
- MODIS-derived SWIR can be used to detect the impacts of water stress on LE

Correspondence to:
Y. Yao,
boyyunjun@163.com

Citation:
Yao, Y., Liang, S., Cao, B., Liu, S., Yu, G., Jia, K., et al. (2018). Satellite detection of water stress effects on terrestrial latent heat flux with MODIS shortwave infrared reflectance data. *Journal of Geophysical Research: Atmospheres*, *123*. https://doi.org/10.1029/2018JD029011

Received 16 MAY 2018
Accepted 8 SEP 2018
Accepted article online 17 SEP 2018

Author Contributions:
Conceptualization: Yunjun Yao
Formal analysis: Yunjun Yao
Methodology: Yunjun Yao, Shaomin Liu, Yuhu Zhang
Validation: Yunjun Yao, Kun Jia
Writing - original draft: Yunjun Yao, Xiaotong Zhang
Writing – review & editing: Yunjun Yao, Shunlin Liang, Bao Cao, Kun Jia, Xiaotong Zhang, Yuhu Zhang, Jiquan Chen, Joshua B. Fisher

Satellite Detection of Water Stress Effects on Terrestrial Latent Heat Flux With MODIS Shortwave Infrared Reflectance Data

Yunjun Yao[1], Shunlin Liang[2], Bao Cao[3], Shaomin Liu[4], Guirui Yu[5], Kun Jia[1], Xiaotong Zhang[1], Yuhu Zhang[6], Jiquan Chen[7], and Joshua B. Fisher[8]

[1]State Key Laboratory of Remote Sensing Science, Faculty of Geographical Science, Beijing Normal University, Beijing, China, [2]Department of Geographical Sciences, University of Maryland, College Park, MD, USA, [3]Chinese Research Academy of Environmental Sciences, Beijing, China, [4]State Key Laboratory of Earth Surface Processes and Resource Ecology, Faculty of Geographical Science, Beijing Normal University, Beijing, China, [5]Synthesis Research Center of Chinese Ecosystem Research Network, Key Laboratory of Ecosystem Network Observation and Modeling, Institute of Geographic Sciences and Natural Resources Research, Chinese Academy of Sciences, Beijing, China, [6]College of Resource Environment and Tourism, Capital Normal University, Beijing, China, [7]Center for Global Changes and Earth Observation/Department of Geography, Environment, and Spatial Sciences, Michigan State University, East Lansing, MI, USA, [8]Jet Propulsion Laboratory, California Institute of Technology, Pasadena, CA, USA

Abstract The MODerate-resolution Imaging Spectroradiometer (*MODIS*) provides spatially contiguous measurements of terrestrial biophysical variables, which can be used to estimate the terrestrial latent heat flux (*LE*). MODIS-derived shortwave infrared reflectance (*SWIR*) metrics (SWIRs) are sensitive to the soil moisture and vegetation water stress. In this study, we used the MODIS-derived SWIRs with eddy covariance flux measurements obtained from 25 flux tower sites representing 10 different land cover types within China to evaluate the sensitivity of SWIRs to ground-measured evaporation fraction and LE. The water constraint metrics determined using the MODIS-derived SWIR generally corresponded better with the ground-measured evaporation fraction values than those obtained without using SWIR. The MODIS-derived SWIRs were used as proxies for the soil and vegetation water supply constraints in a revised Priestley-Taylor algorithm to estimate the terrestrial LE. The estimated LE using the MODIS-derived SWIRs generally corresponded well with the ground-measured LE ($0.56 \leq R^2 \leq 0.97$) for most of the flux tower sites. Regional algorithm sensitivity analysis using the MODIS-derived SWIRs as water supply proxies demonstrated that water limitations reduce LE by more than 53% over China, and the atmospheric vapor pressure deficit and relative humidity are not sufficient to characterize both the atmosphere demand and water supply for LE estimation. Our results demonstrate the potential of using MODIS-derived SWIRs to characterize soil and vegetation water supply factors for determining LE, where the relatively high spatial and temporal resolutions (500 m and daily) are closer to the scale of the eddy covariance ground measurements.

1. Introduction

The terrestrial latent heat flux (*LE*) is the sum of heat flux from soil evaporation, vegetation transpiration, and interception evaporation by vegetation canopies, and it is a key variable linked to energy, water, and carbon exchange among the terrestrial biosphere, hydrosphere, and atmosphere (Fisher et al., 2017; Jung et al., 2010; Monteith, 1965; Mu et al., 2007; K. Wang & Dickinson, 2012; Yao et al., 2013). It is challenging to accurately and reliably obtain the regional or global terrestrial LE due to heterogeneity in the soil and vegetation conditions, as well as the uncertainty in biophysical processes. Since the 1990s, eddy covariance (*EC*) measurements from more than 700 flux tower sites provided by *FLUXNET* projects have been used widely to measure LE at the level of a local tower footprint and with half-hour temporal resolution (Baldocchi et al., 2001; S. Liu et al., 2011). However, a major limitation of these EC measurements for regional LE estimation is their spatial isolation and representation, and sampling error relative to the global scale due to the complex heterogeneity of terrestrial ecosystems (Schimel et al., 2014; Yao et al., 2015; Yuan et al., 2010).

Satellite remote sensing, especially using the MODerate-resolution Imaging Spectroradiometer (*MODIS*), can provide frequent and spatially contiguous measurements of the dynamics of terrestrial biophysical variables, for example, land surface temperature (*LST*) and vegetation index (*VI*), to estimate the regional LE or evapotranspiration (*ET*) (Kalma et al., 2008; Xu et al., 2011; Yao et al., 2014). A classic and alternative satellite-based LE method, the Priestley-Taylor (*PT*) algorithm, employs a coefficient multiplier (the PT parameter, *a*) to reduce the error in LE estimation by avoiding the complex parameterizations of aerodynamic and surface resistance in the Penman-Monteith method (Fisher et al., 2008; Monteith, 1965; Priestley & Taylor, 1972). In general, *a* varies from 0 to 1.26 to reduce potential ET to actual ET with changes in the surface moisture availability and atmospheric demand. Two different modeling methods have been proposed to calculate *a* for estimating the regional LE. One method uses the spatial variation in LST and the normalized difference vegetation index (*NDVI*) in the LST-NDVI triangular/trapezoid spectral space to determine *a* for estimating the evaporation fraction (*EF*; the ratio of LE to available energy) and LE (Jiang & Islam, 2001; Long & Singh, 2012; Yang & Shang, 2013; Zhang et al., 2005). Another method, the PT-JPL algorithm, uses the potential maximum *a* to multiply ecophysiological constraints, including the leaf area index (*LAI*), NDVI, relative humidity (*RH*), and atmospheric vapor pressure deficit (*VPD*, Fisher et al., 2008; Jin et al., 2011; Miralles et al., 2011; Yao et al., 2017). Currently, the PT-JPL algorithm based on ecophysiological constraints is employed for estimating LE for global and regional cropland relative to crop water using LE algorithms to ensure food security in the 21st century.

Terrestrial water vapor and CO_2 exchanges in the soil-plant-atmosphere continuum are affected significantly by the moisture supply from the plant canopy water and soil moisture (*SM*) within different soil profile layers (K. Wang & Dickinson, 2012; J. Xiao et al., 2010; Xu et al., 2016). In the PT-JPL model, RH^{VPD} is used to characterize the impacts of SM on soil evaporation (Fisher et al., 2008). However, RH and VPD only account for the effects of the air moisture concentration and atmospheric evaporation demand, whereas they ignore the impacts of the SM supply, which may lead to large uncertainty in estimation of soil evaporation (ET_s, H. Yan et al., 2012). Many subsequent extensions of the PT models directly use ground-measured or microwave-derived SM to estimate ET_s, but the high spatial resolution SM data required is not regionally available (Dirmeyer et al., 2004; Miralles et al., 2011). In addition, the PT-JPL model includes a plant moisture constraint derived from the fraction of photosynthetically active radiation (PAR) absorbed by green vegetation cover (f_{APAR}) using the satellite visible and near infrared (*VNIR*) bands, but a f_{APAR}-based representation of plant water constraint may lead to large uncertainty in modeled estimates of vegetation transpiration (ET_v) due to the limited ability of f_{APAR} to simulate plant moisture (Ceccato et al., 2001; Yao et al., 2015). Many PT and Penman-Monteith models have successfully parameterized soil and plant moisture constraints using meteorological factors and satellite-based VNIR data, but the comprehensive utilization of VNIR and shortwave infrared reflectance (*SWIR*) for detecting the regional LE responses to surface moisture stress is lacking.

Numerous studies have demonstrated the potential of using satellite-derived SWIR metrics (SWIRs) to improve estimates of the regional LE and gross primary production (*GPP*). The traditional SWIR-based surface moisture indices are the most useful indicators for understanding short-term changes in terrestrial water availability and LE, whereas VNIR-based indices do not reflect them well because the SWIR spectra (1,605–2,105 nm) are sensitive to liquid water in the soil and the vegetation canopy (Ceccato et al., 2001; B. Gao, 1996; Olsen et al., 2015). Previous studies that employed a SWIR-based water stress index or normalized difference water index (*NDWI*) as a VNIR-based NDVI proxy for estimating LE obtained good agreement with ground-measured LE and improved detection of intraseasonal stress (Lu & Zhuang, 2010; Olsen et al., 2013, 2015). MODIS-derived SWIRs coupled with a modified PT algorithm also obtained good agreement with ground-measured LE under a wide variety of conditions (Daniela & Virginia, 2014).

Alternatively, the satellite-derived SWIRs might be regarded as a surface moisture stress index for characterizing the surface water conditions by retrieving the SM and plant water content (D. Chen et al., 2005; Sadeghi et al., 2017, 2015; X. Xiao et al., 2004; Yilmaz et al., 2008). A linear relationship between the transformed reflectance and soil water content in the MODIS SWIR bands was reported by Zarco-Tejada et al. (2003) based on their demonstration that MODIS SWIR band 7 (2105–2155 nm) corresponds to the peak and valley of the surface water absorption curve. Similarly, Sadeghi et al. (2015) used the soil surface reflectance in Landsat SWIR bands to account for more than 70% of the SM moisture variation for different soils based on a combination of the referenced dry soil reflectance and saturated wet soil reflectance. In addition, it has been verified that the integrated SWIR and near infrared (NIR) metrics are sensitive to the variations in the plant water contents caused by environmental water stress, although they are also sensitive to vegetation types and the soil background conditions (X. Xiao et al., 2002). X. Xiao et al. (2004) successfully used a land surface water index (*LSWI*) calculated based on the SWIR and NIR bands to consider the effects of vegetation water stress on plant photosynthesis for estimating the GPP. The time series LSWI could track the seasonal dynamics of the vegetation water stress (X. Xiao et al., 2005). The MODIS-derived SWIRs were also obtained to optimize the canopy conductance associated with vegetation water stress for estimating LE at 16 global FLUXNET sites located in six different biomes (Yebra et al., 2013).

Satellite-derived SWIRs are also sensitive to other environmental factors (e.g., soil texture, vegetation types, and structure), but cloud contamination and differences in the observation view angles of satellite sensors may constrain the utility of satellite-derived SWIRs at regional scales (Barton & North, 2001; Fernández et al., 2015; X. Liu & Liu, 2014). Fortunately, MODIS-derived SWIRs have relatively high spatial and temporal resolutions (~500 m and daily), which promotes the acquisition of biophysical variables. However, the impacts of MODIS-derived SWIRs as the water stress indicators and the environmental control factors on the terrestrial LE remain unclear. Thus, the use of MODIS-derived SWIRs to characterize water supply constraints that affect the terrestrial LE still requires further evaluation for a variety of biomes.

In this study, we investigated the impacts of water stress on the terrestrial LE using MODIS-derived SWIRs as water supply constraints to replace the SM and plant water constraints in a revised PT model. The objectives of this study were (1) to analyze the correlations between MODIS-derived SWIRs and meteorological variables such as the ground-measured SM, EF, and LE; (2) to apply the revised PT algorithm by coupling MODIS-derived SWIRs to evaluate the impacts of water stress on LE; and (3) to map the differences in the mean daily LE (2003–2005) in China according to the estimated LE using the MODIS-derived SWIRs and that estimated without using SWIRs to assess the regional impacts related to SWIRs on the water supply and the terrestrial LE.

2. Data

2.1. Eddy Covariance Data at the Flux Tower Sites

Eddy flux measurements of the surface heat fluxes and the corresponding meteorological data across China were used to assess the performance of the model. Data from 25 EC flux tower sites were provided by the Synergetic Enhanced Observation Network for the arid and semiarid regions of northern China (Hao et al., 2016; Ma et al., 2014; H. Wang et al., 2010; X. F. Wang et al., 2012), Chinaflux (Fu et al., 2006; Guan et al., 2006; Sun et al., 2006; H. Wang et al., 2008; Wen et al., 2006; Yu et al., 2006; G. Y. Zhou et al., 2011), the flux observation experiment of the Haihe River Basin of North China (Jia et al., 2012; S. Liu et al., 2013), the Multiscale Observation Experiment on Evapotranspiration over heterogeneous land surface of the Heihe Water Allied Telemetry Experimental Research of Northwest China (Li et al., 2013; S. Liu et al., 2011; Xu et al., 2013), the Chinese Ecosystem Research Network (R. Liu et al., 2012), and the coordinated Asia-European long-term observing system of Qinghai-Tibet Plateau hydrometeorological processes and the Asian-monsoon system with ground satellite image data and numerical simulations (Ma et al., 2014), which is conducted under the European Commission *FP7* framework and by the individual principal investigators of the FLUXNET network (Wei et al., 2012; Y. Yan et al., 2008; J. Zhou et al., 2011; Table 1 and Figure 1). These flux tower sites include 10 major land cover types: evergreen needleleaf forest (*ENF*), evergreen broadleaf forest (*EBF*), deciduous needleleaf forest (*DNF*), deciduous broadleaf forest (*DBF*), mixed forest (*MIF*), cropland (*CRO*), grassland (*GRA*), open shrubland (*OSH*), desert/barren lands (*BAR*), and wetland (*WET*). The climates covered by these flux tower sites comprised subtropical, temperate, subarctic, and arid zones.

The half-hour data included the surface net radiation (R_n), downward shortwave radiation (R_s), soil heat flux (*G*), LE, sensible heat flux (*H*), air temperature (T_a), RH, atmospheric water pressure (*e*), precipitation (*P*), SM, and wind speed (*WS*). The half-hour turbulent surface heat fluxes and other climate parameters were linearly aggregated into daily, monthly, and annual means. The daily data were set as missing when the amount of missing data exceeded 20% of the reliable half-hourly measurements. Due to the energy imbalance problem, we corrected the LE and *H* using the method developed by Twine et al. (2000). We also used the climatic drought index (Zhang, 1998) calculated as the ratio of potential ET (*PET*) relative to *P* using the ground-measured data to assess the regional impacts of water stress on terrestrial LE. The dry climate conditions comprised five categories: extreme humid ($DI \leq 0.5$), humid ($0.5 < DI \leq 1.0$), subhumid ($1.0 < DI \leq 3.0$), semiarid ($3.0 < DI \leq 7.0$), and arid ($DI > 7.0$).

10.1029/2018JD029011

Table 1
Summary of the 25 Flux Tower Sites Used in This Study, Including the Site Name, Latitude (Lat), Longitude (Lon), Land Cover Types, International Geosphere-Biosphere Programme Land Cover Types (IGBP), Natural Division/Climate, Depth of Soil Moisture (SM), In Situ Upper Layer Soil Water Content (SM_{max} and SM_{min}), Drought Index (DI), Time Period, Project and References

Name	Lat, Lon	Land cover types	IGBP	Natural division/climate	Depth of SM	SMmax (%)	SMmin (%)	DI	Altitude (m)	Time period	Project	Reference
Daxing (DX)	39.62°N, 116.43°E	Winter wheat/maize and vegetables	CRO	NC/Temperate continental monsoon	5 cm	31.81	3.46	2.68	20	2008–2010	Haihe-Flux	Liu et al. (2013)
Guantao (GT)	36.52°N, 115.53°E	Winter wheat/maize and cotton	CRO	NC/Temperate continental monsoon	5 cm	30.05	10.01	1.61	30	2008–2010	Haihe-Flux	Liu et al. (2013)
Jinzhou (JZ)	41.18°N, 121.21°E	Maize	CRO	NC/Temperate continental monsoon	10 cm	33.06	6.96	1.39	22	2008–2009	Asiaflux	Zhang and Zhou (2017)
Miyun (MY)	40.63°N, 117.32°E	Orchard and maize	CRO	NC/Temperate continental monsoon	5 cm	39.37	12.49	1.27	350	2008–2010	Haihe-Flux	Liu et al. (2013)
Tongyu (TY)	44.57°N, 122.88°E	Sunflower	CRO	IM/Temperate semiarid continental	5 cm	29.48	8.36	2.79	184	2008–2009	SEON	H. Wang et al. (2010)
Yucheng (YC)	36.83°N, 116.57°E	Warmer temperate dry farming cropland	CRO	NC/Temperate continental monsoon	20 cm	65.87	32.57	1.54	28	2002–2007	Chinaflux	Sun et al. (2006)
Arou (AR)	38.04°N, 100.46°E	Subalpine meadow	GRA	QT/Alpine	10 cm	47.16	31.46	1.46	3033	2008–2009	SEON	Wang et al. (2012)
Fukang (FK)	44.28°N, 87.92°E	Desert steppe	GRA	NWC/Arid and semiarid, temperate continental	10 cm	32.01	13.95	7.20	482	2006–2007	CERN	Liu et al. (2012)
Inner Mongolia (NMG)	44.50°N, 117.17°E	Typical steppe and meadow steppe	GRA	IM/Temperate semiarid continental	5 cm	27.62	5.72	3.84	1189	2003–2007	Chinaflux	Fu et al. (2006)
Linzhi (LZ)	29.77°N, 94.74°E	Alpine grassland	GRA	QT/Highland continental	5 cm	35.27	15.41	0.78	3324	2008–2010	CEOP-AEGIS	Ma et al. (2014)
Maqu (MQ)	33.89°N, 102.14°E	Grassy marshland	GRA	QT/Highland continental	5 cm	25.62	2.13	1.21	3423	2009–2010	SEON	Ma et al. (2014)
Nagqu (NQ)	31.37°N, 91.90°E	Alpine steppe	GRA	QT/Highland continental	5 cm	33.98	14.71	2.13	4509	2008–2011	CEOP-AEGIS	Ma et al. (2014)
Nam Co (NaC)	30.77°N, 90.96°E	Alpine steppe	GRA	QT/Highland continental	5 cm	36.13	18.11	2.03	4730	2008–2010	CEOP-AEGIS	Li et al. (2015)
Qingyang (QY)	35.59°N, 107.54°E	Grass	GRA	NC/Temperate continental monsoon	5 cm	36.01	13.81	2.01	1095	2009	SEON	Hao et al. (2016)
Dinghushan (DHS)	23.17°N, 112.54°E	Evergreen broadleaf forest	EBF	SC/Monsoon humid	5 cm	31.73	16.50	0.49	240	2002–2007	Chinaflux	G. Y. Zhou et al. (2011)
Huaining (HN)	33.00°N, 117.00°E	Deciduous broadleaf forests	DBF	NC/Temperate continental monsoon	15 cm	39.37	24.88	1.15	23	2005–2006	FLUXNET	J. Zhou et al. (2011)
Yueyang (YY)	29.31°N, 112.51°E	Poplar plantation	DBF	CC/Subtropical monsoon	5 cm	41.45	28.48	0.98	31	2005–2006	FLUXNET	Wei et al. (2012)
Xishuangbanna (XSBN)	21.95°N, 101.27°E	Tropical seasonal rain forest	EBF	SC/Typical monsoon humid	5 cm	28.73	10.14	0.79	756	2002–2004	*Chinaflux*	Yu et al. (2006)
Laoshan (LSH)	45.28°N, 127.58 °E	Larch forest	DNF	NEC/Cool temperate	5 cm	24.54	4.80	0.99	340	2003–2007	Chinaflux	Wang et al. (2008)
Qianyanzhou (QYZ)	26.74°N, 115.05°E	Typical subtropical monsoon man-planted forest	ENF	CC/Subtropical monsoon	5 cm	39.86	22.72	0.65	102	2002–2007	Chinaflux	Wen et al. (2006)
Changbaishan (CBS)	42.40°N, 128.10°E	Temperate mixed forest	MIF	NEC/Cool temperate	20 cm	68.09	14.11	0.92	761	2002–2007	Chinaflux	Guan et al. (2006)
Haibei (HB)	37.62°N, 101.32°E	Typical frigid vegetation	OSH	QT/Highland continental	20 cm	53.50	6.25	0.80	3250	2002–2007	Chinaflux	Fu et al. (2006)
Dongtan (DT)	31.58°N, 121.90°E	Coastal salt marsh	WET	CC/Subtropical monsoon	5 cm	98.20	45.60	1.37	5	2005	FLUXNET	Yan et al. (2008)
Huazhaizi (HZZ)	38.77°N, 100.32°E	Desert	BAR	NWC/arid and semiarid, temperate continental	2 cm	40.03	0.01	4.92	1731	2012–2015	HiWATER- MUSOEXE	Liu et al. (2011)
Shenshawo (SSW)	38.79°N, 100.49°E	Desert	BAR	NWC/Arid and semiarid, temperate continental	2 cm	11.02	2.38	4.81	1594	2012–2015	HiWATER-MUSOEXE	Liu et al. (2011)

Note. NEC = northeast China; NC = north China; CC = central China; SC = south China; IM = Inner Mongolia; NWC = northwest China; QT = Qinghai-Tibet region; WAT = water body; ENF = evergreen needleleaf forest; EBF = evergreen broadleaf forest; DNF = deciduous needleleaf forest; DBF = deciduous broadleaf forest; MIF = mixed forest; CSH = closed shrubland; OSH = open shrubland; GRA = grassland; WET = permanent wetland; CRO = cropland; URB = urban/buildup; CNV = cropland/natural vegetation mosaic; SNI = snow/ice; BAR = barren lands; CEOP-AEGIS = Coordinated Asia-European long-term Observing system of Qinghai-Tibet Plateau hydrometeorological processes and the Asian-monsoon systEm with Ground satellite Image data and numerical Simulations; SM = soil moisture. SM_{max} was derived as the SM value in 1 year after a strong rainfall event, and SM_{min} was set as the minimum value in the dry season using the ground-measured data for the study period.

10.1029/2018JD029011

2.2. MODIS Data

To evaluate LE model at the site scales, we used the daily 500-m resolution Terra MODIS surface reflectance product (*MCD43A*; Collection V006, Z. S. Wang et al., 2018) from 2000 to 2012 to acquire SWIRs. MCD43A includes seven bands: band 1 (red: 620–670 nm), band 2 (*NIR*: 841–876 nm), band 3 (blue: 459–479 nm), band 4 (green: 545–565 nm), band 5 (NIR: 1,230–1,250 nm), band 6 (SWIR: 1,638–1,652 nm), and band 7 (SWIR: 2,105–2,135 nm). The daily 250-m resolution MODIS cloud mask product (*MOD35_L2*) was used to remove the surface reflectance product with high cloud cover (Goerner et al., 2011), and the daily cloud mask product was linearly interpolated to 500 m. Based on the geolocation information for the flux tower sites, the daily SWIRs with 500-m spatial resolution were extracted from MODIS surface reflectance product over each flux tower site.

To estimate the regional LE in China, we also used the 500-m resolution International Geosphere-Biosphere Programme land cover types from the MODIS product (*MCD12Q1*, Friedl et al., 2002) for 2004 to represent land cover information. In addition, the 16-day MODIS collection five surface Bidirectional Reflectance Distribution Function/albedo product at a 500-m spatial resolution (Lucht et al., 2000) for the period of 2003–2005 was also used to calculate R_n, and the daily albedo values were linearly interpolated from the 16-day averages at the temporal scale.

2.3. Regional Meteorological Data

The regional averaged daily LE was estimated in China using the revised PT algorithm and daily gridded near-surface meteorological data from the Environmental and Ecological Science Data Center for West China (Y. Chen et al., 2011; Yang et al., 2010). The daily gridded meteorological data with a spatial resolution of 0.1° were acquired for the period of 1982–2015, including R_s, T_a, maximum daily air temperature ($T_{\max}$), minimum daily air temperature ($T_{\min}$), RH, e, and WS. The gridded data sets were produced by fusing Global Energy and Water Cycle Experiment Surface Radiation Budget products, Global Land Data Assimilation System data, Princeton reanalysis data, and ground-measured meteorological variables provided by the China Meteorological Administration (He & Yang, 2011). The daily gridded meteorological data were spatially interpolated to 500 m using the bilinear interpolation method.

3. Methods

3.1. MODIS-Derived SWIR Metrics

Two MODIS-based SWIRs were used to drive the revised PT algorithm for terrestrial LE estimation. The first SWIR index employed was the SWIR SM index (*SMI*) used to characterize the variation in SM for bare soil (He & Kobayashi, 1998; Sadeghi et al., 2015; Zarco-Tejada et al., 2003), which is defined as

$$\mathrm{SMI} = \frac{\rho_{swir,d} - \rho_{swir,s}}{\rho_{swir,d} - \rho_{swir,w}}, \quad (1)$$

where $\rho_{\mathrm{swir},d}$, $\rho_{\mathrm{swir},s}$, and $\rho_{\mathrm{swir},w}$ are the reflectances of the dry soil, regular soil, and saturated soil in the SWIR bands (band 7 in the MODIS data), respectively. In this study, $\rho_{\mathrm{swir},d}$ and $\rho_{\mathrm{swir},w}$ were determined as 0.75 and 0.001 based on our ground measurements. Assuming that the pixel only includes two end-members (vegetation and bare soil), the satellite-derived reflectance ($\rho_{\mathrm{swir},7}$) of the mixed pixel in the SWIR bands (band 7 in the MODIS data) is considered to be a linear combination of the $\rho_{\mathrm{swir},s}$ and the reflectance of vegetation ($\rho_{\mathrm{swir},c}$).

$$\rho_{swir,s}[1 - f(g)] + \rho_{swir,c} f(g) = \rho_{swir,7} \quad (2)$$

and

$$\rho_{swir,s} = \frac{\rho_{swir,7} - \rho_{swir,c} f(g)}{1 - f(g)}, \quad (3)$$

where *f*(*g*) is the green canopy fraction, which can be calculated based on a simple empirical equation using NDVI data (Carlson & Ripley, 1997; Fisher et al., 2008). In this study, $\rho_{\mathrm{swir},c}$ was determined as 0.10 based on our ground measurements.

10.1029/2018JD029011

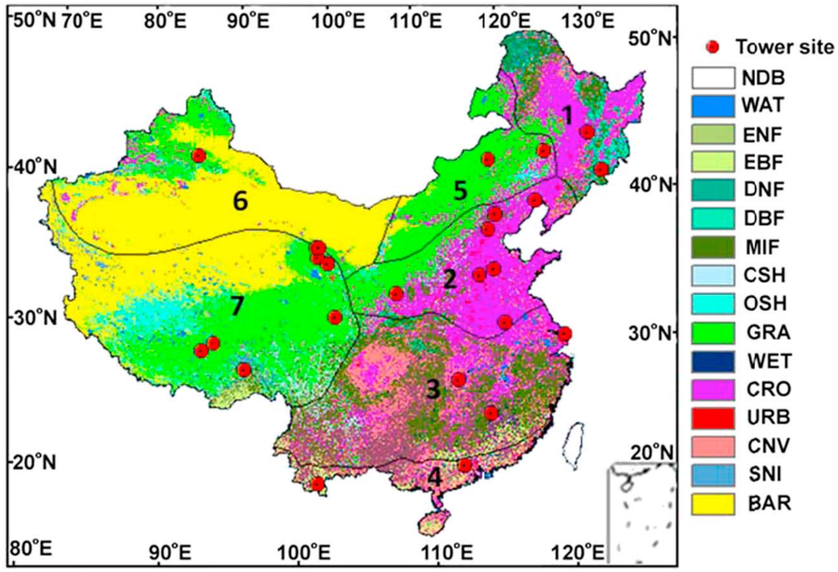

Figure 1. Locations of 25 flux tower sites used in this study and 7 natural divisions of mainland China. The natural divisions are 1. Northeast China; 2. North China; 3. Central China; 4. South China; 5. Inner Mongolia; 6. northwest China; and 7. Qinghai-Tibet region. NDB refers to natural division boundary. The background image shows the land cover product for 2004 from the MODIS land cover (MOD12) product. WAT = water body; ENF = evergreen needleleaf forest; EBF = evergreen broadleaf forest; DNF = deciduous needleleaf forest; DBF = deciduous broadleaf forest; MIF = mixed forest; CSH = closed shrubland; OSH = open shrubland; GRA = grassland; WET = wetland; CRO = crop land; URB = urban/buildup; CNV = crop land/natural vegetation mosaic; SNI = snow/ice; BAR = barren lands; MODIS = MODerate-resolution Imaging Spectroradiometer.

The second SWIR index employed was the LSWI proposed by X. Xiao et al. (2002), which uses the NIR and SWIR bands to reflect vegetation canopy water stress. LSWI is calculated as

$$LSWI = \frac{\rho_{\mathrm{nir}} - \rho_{swir,6}}{\rho_{\mathrm{nir}} + \rho_{swir,6}}, \tag{4}$$

where ρ_{nir} and $\rho_{\mathrm{swir,6}}$ represent the reflectance of the NIR (band 2 in the MODIS data) and SWIR (band 6 in the MODIS data) bands, respectively.

3.2. Revised PT Algorithm Framework

The terrestrial LE was estimated based on the satellite-based PT algorithm (PT-JPL) framework (Fisher et al., 2008; Priestley & Taylor, 1972) as

$$LE = LE_s + LE_c + LE_i, \tag{5}$$

$$LE_s = \alpha(1 - f_{\mathrm{wet}})f(SM)\frac{\Delta}{\Delta + \gamma}(R_{\mathrm{ns}} - G), \tag{6}$$

$$LE_c = \alpha(1 - f_{\mathrm{wet}})f(g)f(T)f(\mathrm{CM})\frac{\Delta}{\Delta + \gamma}R_{\mathrm{nc}}, \tag{7}$$

and

$$LE_i = \alpha f_{\mathrm{wet}}\frac{\Delta}{\Delta + \gamma}(R_n - G), \tag{8}$$

where LE_s is the LE for soil evaporation, LE_c is the LE for vegetation canopy transpiration, LE_i is the LE for interception evaporation, *a* is the PT parameter (1.26), f_{wet} is the wet surface fraction (RH^4), Δ is the slope of the saturated vapor pressure curve, γ is the psychrometric constant, and R_{ns} and R_{nc} are the surface net radiation (R_n) partitioned to the soil and vegetation canopy, respectively. *G* is the soil heat flux, *f*(*T*) is the plant temperature constraint ($\exp\{-[(T_a - T_{opt})/T_{opt}]^2\}$), T_{opt} is the optimum air temperature (25 °C), f (SM) is the SM constraint, and f (CM) is the plant moisture constraint.

At the site scale, we directly used ground-measured R_n, G, T_a, and RH to drive the satellite-based PT-JPL for LE estimation. At the regional scale, R_n was obtained based on the method given by Allen et al. (1998)

$$R_{\mathrm{n}} = R_s(1 - \partial) - R_{\mathrm{nl}} \tag{9}$$

and

$$R_{\mathrm{nl}} = \delta\left[\frac{(T_{\max} + 273.15)^4 + (T_{\min} + 273.15)^4}{2}\right]\left(0.34 - 0.14\sqrt{e}\right)\left(1.35\frac{R_s}{R_{s0}} - 0.35\right), \tag{10}$$

where ∂ is the surface albedo, δ is the Stefan-Boltzmann constant (4.903×10^{-9} MJ/[K^4·m^2·d]), and R_{s0} is the clear-sky incoming shortwave radiation (W/m^2). Regional G was calculated using a simple empirical algorithm provided by Yao et al. (2013)

$$\mathrm{G} = \alpha_g[1 - f(g)]R_n, \tag{11}$$

where a_g is an empirical coefficient and is set as 0.18 herein (Yao et al., 2013).

In general, f (SM) can be defined as ($\mathrm{SM} - \mathrm{SM}_{\min}$)/($\mathrm{SM}_{\max} - \mathrm{SM}_{\min}$), where $\mathrm{SM}_{\max}$ and $\mathrm{SM}_{\min}$ represent the maximum and minimum SM, respectively. $\mathrm{SM}_{\max}$ was set as the value of SM in 1 year after a strong rainfall event, and $\mathrm{SM}_{\min}$ was derived from the minimum value in the dry season using the ground-measured data for the study period (Garcia et al., 2013; Morillas et al., 2013). In the original PT-JPL model, f (SM) uses an indicator of the atmospheric evaporative demand ($\mathrm{RH}^{\mathrm{VPD}}$) as a proxy for SM. In the present study, we considered the effects of the atmospheric evaporative demand and surface SM supply on $\mathrm{LE_s}$ (He & Kobayashi, 1998), where the response of $\mathrm{LE_s}$ to SM stress was defined as

$$f(SM) = (\mathrm{SMI}\times\mathrm{RH})^{\mathrm{RHD}/\beta}, \tag{12}$$

where SMI is the SWIR SMI described in section 3.1, *RHD* is the relative humidity deficit (1 – RH; K. Wang et al., 2010), and β is a fixed parameter (0.50).

f (CM) was calculated using the relative variation in light absorbance ($f_{\mathrm{APAR}}/f_{\mathrm{APARmax}}$) in the original PT-JPL model, but the validation also demonstrated the usefulness of the LSWI for improving estimate of the canopy water content and LE for a variety of biomes (Maki et al., 2004; Olsen et al., 2015; X. Xiao et al., 2005). Wu et al. (2010) further found that the product of $VI \times VI$ improved estimates of the canopy water content and GPP. In this study, we followed X. Xiao et al. (2005) and Wu et al. (2010) and define f (CM) as

$$f(\mathrm{CM}) = \frac{CMI}{CMI_{\max}} \tag{13}$$

and

$$CMI = NDVI\sqrt{1 + LSWI}, \tag{14}$$

where *CMI* is the vegetation canopy water index, $\mathrm{CMI}_{\max}$ is the maximum CMI, and we select the maximum CMI value within the vegetation growing season for single pixels as an estimate of $CMI_{\max}$.

3.3. Assessment Methods

To identify the capacity of MODIS-derived SWIRs to represent water supply constraints in the revised PT algorithm, we used the squared correlation coefficient (R^2) between different moisture constraint metrics shown in Table 2 and the ground-measured EF across all flux tower sites to analyze the sensitivity of the revised PT algorithm-derived daily terrestrial EF and LE to water constraints. In addition, the LE values estimated using different moisture constraint metrics (LE_swir using both f (sm)_swir and f (cm)_swir; LE_sm using both f (sm) _sm and f (cm)_fapar; and LE_no using both f (sm)_no and f (cm)_no) were compared with the ground-

Table 2
Formulations for Different Water Constraint Metrics Used in This Study From MODIS-Derived SWIRs and Meteorological Variables

Water constraint metrics	Formula
f (sm)_swir	$(RH \times SMI)^{RHD/\beta}$
f (sm)_sm	$\frac{SM - SM_{min}}{SM_{max} - SM_{min}}$
f (sm)_no	$RH^{RHD/\beta}$
f (cm)_swir	$\frac{NDVI\sqrt{1+LSWI}}{\left(NDVI\sqrt{1+LSWI}\right)_{max}}$
f (cm)_fapar	$\frac{f_{APAR}}{f_{APARmax}}$
f (cm)_no	$\frac{NDVI}{NDVI_{max}}$

Note. $f_{APARmax}$ and $NDVI_{max}$ refer to the maximum f_{APAR} and NDVI within the vegetation growing season for single pixels, respectively. NDVI = normalized difference vegetation index; LSWI = land surface water index.

measured values to assess the performance of the model and the effects of the water supply constraints on LE. The performance of the model was evaluated using R^2, the root-mean-squared error (*RMSE*), and the bias of the estimation and observations. RMSE represents the closeness of the simulation and ground measurements, and it is expressed as

$$RMSE = \sqrt{\frac{1}{n}\sum_{i=1}^{n}(S_i - M_i)^2}, \quad (15)$$

where S_i is the simulated value for sample *i*, M_i is the ground-measured value for sample *i*, and *n* is the number of samples.

The spatial pattern in the mean daily LE (2003–2005) difference percentage (*ΔLE*) in China between the estimated LE (LE_swir) determined by employing the MODIS-derived SWIRs and that (LE_no) without using SWIRs was obtained according to the following method:

$$\Delta LE = \frac{LE_{swir} - LE_{no}}{LE_{no}} \times 100\%. \quad (16)$$

4. Results

4.1. Sensitivity of MODIS-Derived SWIRs to Ground-Measured EF and LE

Several moisture constraint metrics comprising three SM constraint metrics (*f* (sm)_swir, *f* (sm)_sm, and *f* (sm)_no) and three SM-related vegetation canopy moisture constraint metrics (*f* (cm)_swir, *f* (cm)_fapar, and *f* (cm)_no) were calculated using MODIS-derived SWIRs and ground-measured RH and SM (Table 3).

Table 3
Squared Correlation Coefficients (R^2) Between Different Moisture Constraint Metrics Shown in Table 2 and Ground-Measured EF Across All the Flux Tower Sites

Name	IGBP	f (sm)_swir	f (sm)_sm	f (sm)_no	f (cm)_swir	f (cm)_fapar	f (cm)_no
DX	CRO	0.38	0.42	0.27	0.58	0.49	0.50
GT	CRO	0.26	0.17	0.18	0.29	0.21	0.22
JZ	CRO	0.49	0.27	0.38	0.60	0.54	0.52
MY	CRO	0.58	0.38	0.49	0.63	0.56	0.57
TY	CRO	0.52	0.46	0.45	0.58	0.51	0.50
YC	CRO	0.33	0.24	0.24	0.57	0.50	0.49
AR	GRA	0.35	0.14	0.16	0.51	0.45	0.45
FK	GRA	0.21	0.16	0.12	0.19	0.11	0.10
NMG	GRA	0.30	0.21	0.22	0.34	0.26	0.26
LZ	GRA	0.33	0.24	0.22	0.27	0.17	0.15
MQ	GRA	0.79	0.69	0.62	0.82	0.73	0.72
NQ	GRA	0.61	0.42	0.52	0.58	0.49	0.47
NaC	GRA	0.34	0.18	0.25	0.41	0.32	0.31
QY	GRA	0.29	0.15	0.21	0.28	0.19	0.20
HN	DBF	0.40	0.30	0.28	0.33	0.23	0.22
YY	DBF	0.23	0.15	0.14	0.28	0.19	0.20
DHS	EBF	0.27	0.16	0.17	0.23	0.16	0.15
XSBN	EBF	0.23	0.15	0.11	0.21	0.12	0.12
LSH	DNF	0.66	0.42	0.56	0.58	0.50	0.49
QYZ	ENF	0.24	0.25	0.13	0.24	0.16	0.15
CBS	MIF	0.47	0.22	0.36	0.41	0.32	0.32
HB	OSH	0.57	0.40	0.42	0.83	0.73	0.72
DT	WET	0.25	0.27	0.16	0.37	0.28	0.27
HZZ	BAR	0.44	0.25	0.35	0.23	0.16	0.15
SSW	BAR	0.53	0.42	0.40	0.43	0.34	0.36

Note. CRO = cropland; GRA = grassland; DBF = deciduous broadleaf forest; EBF = evergreen broadleaf forest; DNF = deciduous needleleaf forest; ENF = evergreen needleleaf forest; MIF = mixed forest; OSH = open shrubland; WET = wetland; BAR = barren lands; IGBP = International Geosphere-Biosphere Programme; EF = evaporation fraction.

Among the three SM constraint metrics, the ground-measured EF estimates generally had the highest correspondence with *f* (sm)_swir ($0.21 < R^2 < 0.79$) for most of the flux tower sites (except for Daxing, Qianyanzhou, and Dongtan), with *f* (sm)_sm ($0.15 < R^2 < 0.69$) was second best, and *f* (sm)_no ($0.11 < R^2 < 0.62$) had the worst performance at these flux tower sites. Similarly, for the three SM-related vegetation canopy water constraint metrics, the *f* (cm)_swir results also accounted for the greatest proportion of the daily variability in EF for most of the flux tower sites (Table 3). Overall, both the *f* (sm)_swir and *f* (cm)_swir had the highest potential capacity for determining the EF seasonality over a variety of land cover and environmental status types.

Figure 2 shows an example of the seasonal variations in the MODIS-derived *f* (sm)_swir and ground-measured *f* (sm)_sm, and EF for different typical flux tower sites. The *f* (sm)_swir was generally proportional to ground-measured EF, and both metrics indicated similar seasonal variations under different land cover types and climate zones. However, the responses of EF to variations in *f* (sm)_sm were relatively complex according to the different climatic moisture gradients. *f* (sm)_sm exhibited large fluctuations, whereas the dynamics of EF and *f* (sm)_swir were relatively small during the growing season at forest (DBF, EBF, DNF, ENF, and MIF) sites, which was consistent with deep soil water extraction via transpiration by actively growing vegetation. However, the variations in both EF and *f* (sm)_swir were only weakly consistent with the variability in *f* (sm)_sm at OSH and WET sites because no water stress occurred at these sites. In addition, both *f* (sm)_swir and EF exhibited evidence of shifts to a response to seasonal *f* (sm)_sm variability at the semiarid and arid GRA, CRO, and BAR sites, and these results were consistent with the SM-related constraints to terrestrial LE at these flux tower sites. An example of the similar seasonal dynamics of the MODIS-derived *f* (cm)_swir and *f* (cm)_fapar, and the ground-measured EF are also shown in Figure 3. Both *f* (cm)_swir and *f* (cm)_fapar corresponded well with EF during seasonal periods at most of the flux tower sites, which was consistent with the vegetation indices used for characterizing the available vegetation canopy water contents.

The distributions of flux tower site correlation coefficients (*r*) between the ground-measured LE and *f* (sm) _swir, f (sm)_sm, and *f* (sm)_no along the climatic dryness status indicated by the climatic drought index (*DI*) are shown in Figure 4. To reduce the impacts of higher seasonal frequency variations, we calculated the correlations using the mean monthly composites of the daily values. The LE values were all positively correlated with *f* (sm)_swir, f (sm)_sm, and *f* (sm)_no, and the correlations were larger as *DI* increased (from 0.49 through 7.20). However, at the same *DI* values, the correlations between *f* (sm)_swir and LE were slightly larger than the correlations between *f* (sm)_sm and LE for most of the flux tower sites, and the smallest correlations were between *f* (sm)_no and LE at these sites.

4.2. Impacts of Water Stress on LE Estimates Across Different Multiple Biomes

Three sets of revised PT algorithm simulations were conducted using tower meteorology at different flux tower sites. The ground-measured SM, RH, and MODIS-derived SWIR observations were used as different water constraint inputs to estimate the daily LE at each flux tower site (LE_swir, LE_sm, and LE_no). Table 4 shows that the LE_swir estimates generally corresponded better with the ground-measured LE than LE_sm or LE_no for most of the flux tower sites. For the CRO (except for both Daxing and Jinzhou), GRA, and BAR sites, the LE_swir results present 6% to 20% greater R^2 ($p < 0.01$) correspondence, as well as 7% to 23.9% lower RMSE differences compared with the ground-measured LE relative to the LE_sm results because SM was generally expected to impose a stronger limitation on LE in these relatively drier regions. For all the forest (DBF, EBF, DNF, ENF, and MIF) flux tower sites, LE_swir exhibited slightly better performance compared to the ground measurements than LE_sm, as indicated by the approximately 8.7% higher R^2 value ($p < 0.01$) and 9.8% smaller RMSE. Similarly, the LE_swir results were 6.7% better in terms of R^2 ($p < 0.01$) than LE_no at these flux tower sites, thereby indicating that the MODIS-derived SWIRs successfully captured the vegetation canopy water content under dense vegetation conditions. In addition, the LE_swir results were improved relative to LE_sm or LE_no at the OSH and WET flux tower sites, as indicated by the higher R^2 value and smaller RMSE.

Figure 5 shows the superior capacity of the three modified PT algorithms driven by tower meteorology for estimating the spatial variation in LE. The RMSE of the site-averaged LE_swir estimates driven by tower meteorology versus the ground-measured LE for different biomes at 25 sites was 14.2 W/m^2, and R^2 was

10.1029/2018JD029011

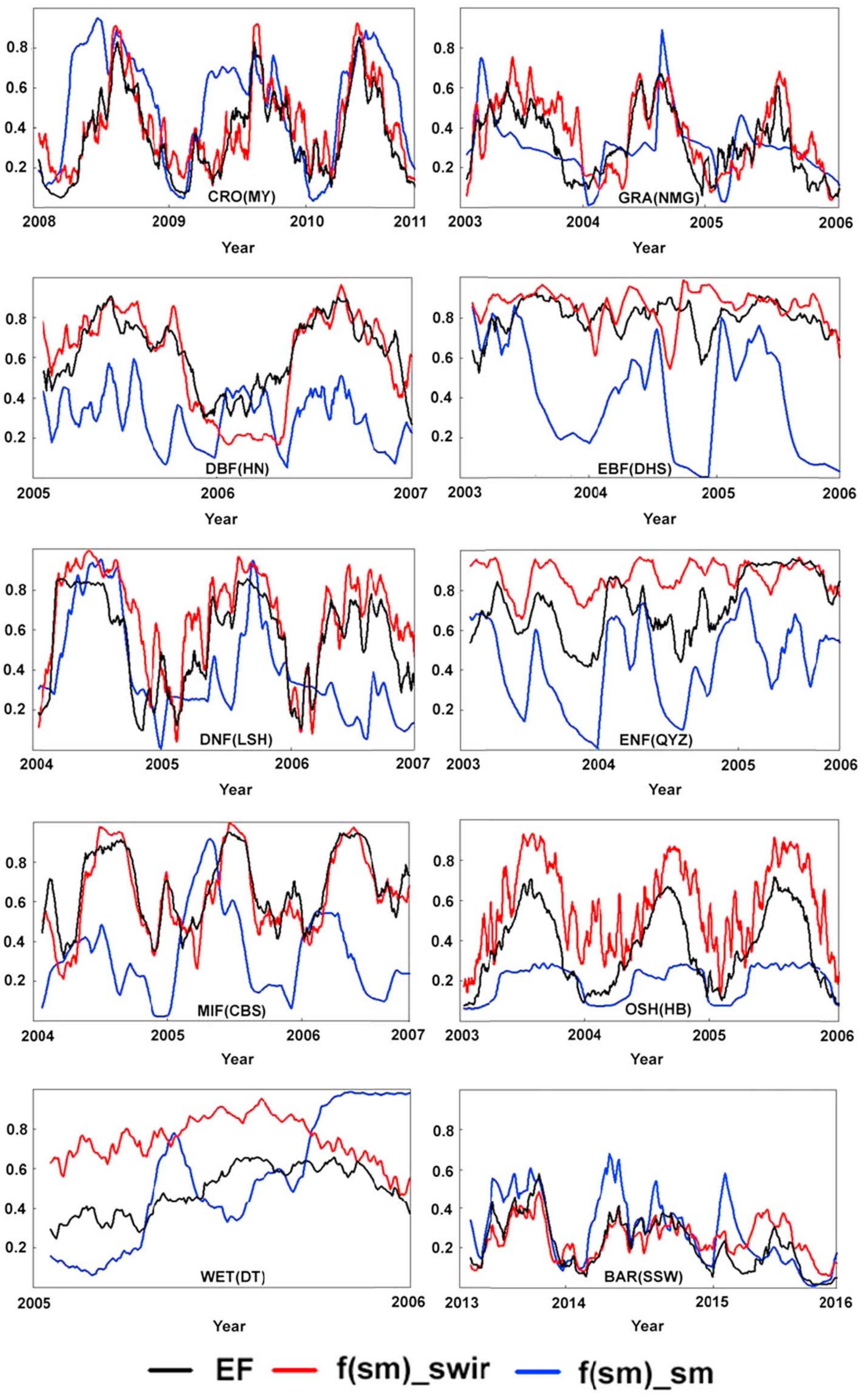

Figure 2. Examples of seasonal ground-measured EF, *f* (sm)_swir and *f* (sm)_sm results for 10 sites. Ten-day moving averages of the daily ground observations are shown for the selected study periods. CRO = crop land; GRA = grassland; DBF = deciduous broadleaf forest; EBF = evergreen broadleaf forest; DNF = deciduous needleleaf forest; ENF = evergreen needleleaf forest; MIF = mixed forest; OSH = open shrubland; WET = wetland; BAR = barren lands. MY = Miyun; NMG = Inner Mongolia; HN = Huaining; DHS = Dinghushan; LSH = Laoshan; QYZ = Qianyanhzou; CBS = Changbaishan; HB = Haibei; DT = Dongtan; SSW = Shenshawo.

10.1029/2018JD029011

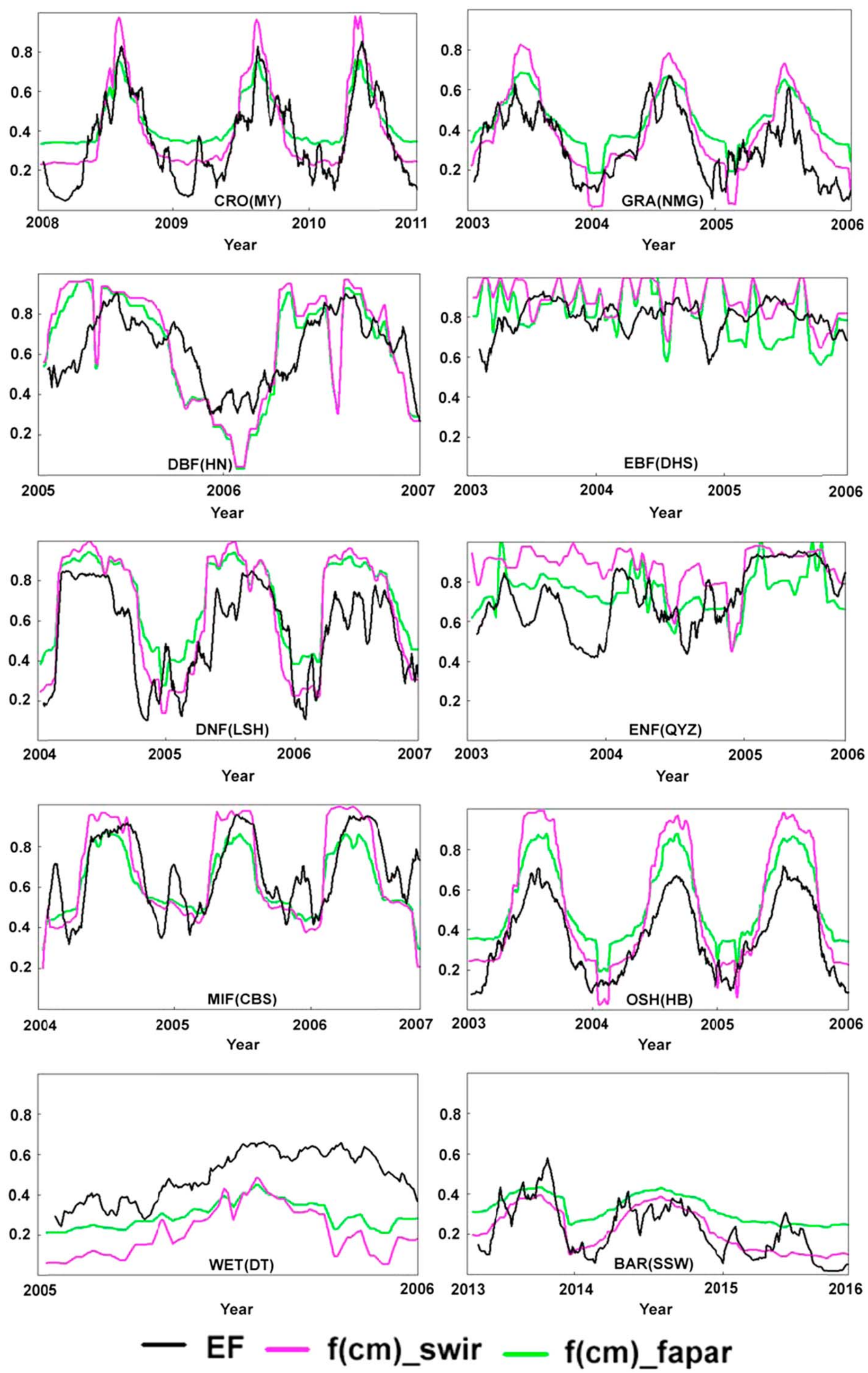

Figure 3. Examples of seasonal ground-measured EF, *f* (cm)_swir and *f* (cm)_fapar results for 10 sites. Ten-day moving averages of the daily ground observations are shown for the selected study period. CRO = cropland; GRA = grassland; DBF = deciduous broadleaf forest; EBF = evergreen broadleaf forest; DNF = deciduous needleleaf forest; ENF = evergreen needleleaf forest; MIF = mixed forest; OSH = open shrubland; WET = wetland; BAR = barren lands. MY = Miyun; NMG = Inner Mongolia; HN = Huaining; DHS = Dinghushan; LSH = Laoshan; QYZ = Qianyanhzou; CBS = Changbaishan; HB = Haibei; DT = Dongtan; SSW = Shenshawo.

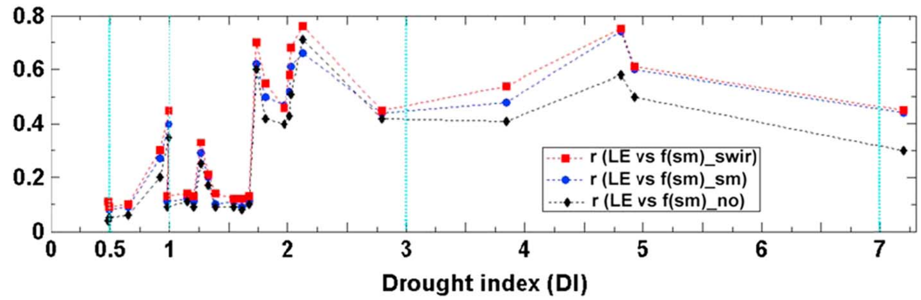

Figure 4. Plots of flux tower site correlation coefficients (*R*) between the ground-measured LE and *f* (sm)_swir, *f* (sm)_sm, and *f* (sm)_no. The flux tower site correlations are distributed along the climatic dryness status indicated by a climatic drought index (*DI*). The *DI* comprises five categories: extreme humid ($DI \leq 0.5$); humid ($0.5 < DI \leq 1.0$); subhumid ($1.0 < DI \leq 3.0$); semiarid ($3.0 < DI \leq 7.0$); and arid ($DI > 7.0$). LE = latent heat flux.

0.85 ($p < 0.01$), thereby indicating that the performance was better than the LE_sm results (RMSE = 22.3 W/m^2, R^2 = 0.78, $p < 0.01$) and the LE_no results (RMSE = 16.9 W/m^2, R^2 = 0.80, $p < 0.01$). Overall, the use of MODIS-derived SWIRs as the water supply constraints in the revised PT algorithm improved the algorithm's performance compared with the alternative LE estimation methods using the ground-measured SM inputs (LE_sm) or without the SWIRs-based water supply constraint (LE_no) for most of the flux tower sites representing different land cover types.

Table 4

Comparisons of the Estimated LE Using Different Moisture Constraint Metrics: LE_swir Using Both f (sm)_swir and f (cm)_swir; LE_sm Using Both f (sm)_sm and f (cm)_fapar; and LE_no Using Both f (sm)_no and f (cm)_no; and Ground-Measured LE Across Different Flux Tower Sites

		LE_swir			LE_sm			LE_no		
Name	IGBP	R^2	RMSE	bias	R^2	RMSE	bias	R^2	RMSE	bias
DX	CRO	0.75	38.2	−20.2	0.76	37.1	−16.8	0.68	41.6	−19.1
GT	CRO	0.81	28.6	−14.7	0.75	30.6	−15.9	0.72	30.1	−13.9
JZ	CRO	0.68	30.9	−3.1	0.69	39.1	−27.3	0.61	33.5	−5.9
MY	CRO	0.84	27.3	−10.8	0.74	35.4	8.9	0.76	29.4	−10.5
TY	CRO	0.80	29.1	−5.2	0.74	34.4	−15.7	0.73	31.8	−2.2
YC	CRO	0.86	17.5	−5.8	0.76	24.5	−13.5	0.77	19.5	−4.7
AR	GRA	0.94	30.4	−26.3	0.84	54.3	−41.4	0.85	43.4	−26.0
FK	GRA	0.56	29.7	5.1	0.50	31.8	0.48	0.42	32.6	12.6
NMG	GRA	0.78	12.5	1.1	0.71	14.3	2.7	0.72	15.9	7.8
LZ	GRA	0.91	20.2	−15.1	0.82	27.8	−22.2	0.83	22.5	−16.1
MQ	GRA	0.97	18.2	−13.7	0.89	25.2	−19.1	0.90	19.4	−13.1
NQ	GRA	0.85	29.8	−23.6	0.77	33.2	−25.1	0.78	32.3	−22.4
NaC	GRA	0.71	26.1	−18.3	0.60	34.5	−21.3	0.65	28.2	−17.6
QY	GRA	0.92	32.8	−27.1	0.86	38.2	−30.6	0.85	34.5	−23.3
HN	DBF	0.82	25.8	1.1	0.72	45.8	−17.5	0.74	27.3	1.3
YY	DBF	0.87	24.6	8.9	0.71	40.2	−10.4	0.76	26.1	9.7
DHS	EBF	0.82	19.5	5.9	0.74	20.9	−9.4	0.75	22.5	6.8
XSBN	EBF	0.78	25.4	−4.5	0.71	28.9	−12.3	0.72	29.6	−4.1
LSH	DNF	0.86	23.7	−14.4	0.79	32.3	−23.4	0.80	26.5	−14.2
QYZ	ENF	0.87	19.8	4.7	0.78	23.7	−8.3	0.79	22.2	5.1
CBS	MIF	0.89	25.3	−18.7	0.80	32.1	−25.2	0.81	27.1	−17.7
HB	OSH	0.93	16.1	−10.7	0.88	25.4	−18.6	0.87	18.9	−10.1
DT	WET	0.61	50.6	23.8	0.55	49.8	18.6	0.54	53.9	25.5
HZZ	BAR	0.74	18.7	−8.1	0.54	26.5	4.8	0.65	21.8	3.9
SSW	BAR	0.85	9.6	−0.1	0.77	16.8	8.4	0.78	12.9	6.9

Note. All of the statistics were calculated at the 99% confidence level. Units for both RMSE and bias are all W/m^2. CRO = cropland; GRA = grassland; DBF = deciduous broadleaf forest; EBF = evergreen broadleaf forest; DNF = deciduous needleleaf forest; ENF = evergreen needleleaf forest; MIF = mixed forest; OSH = open shrubland; WET = wetland; BAR = barren lands; IGBP = International Geosphere-Biosphere Programme; LE = latent heat flux; RMSE = root-mean-squared error.

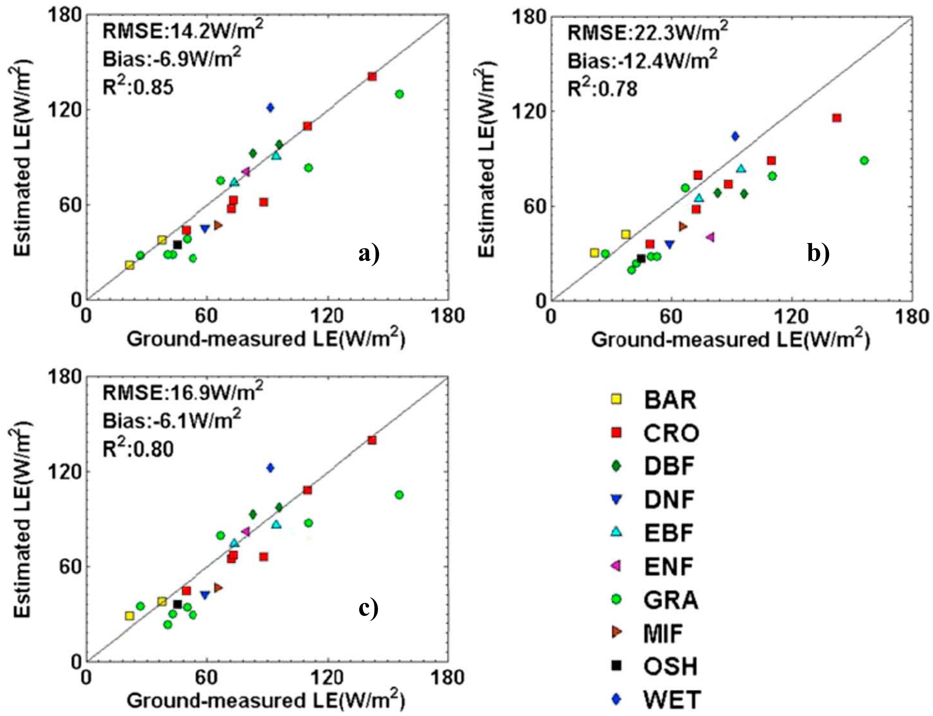

Figure 5. Comparisons of the estimated (a) LE_swir, (b) LE_sm, and (c) LE_no using tower meteorology and measured site averaged daily LE values for different biomes at 25 sites. LE = latent heat flux; CRO = cropland; GRA = grassland; DBF = deciduous broadleaf forest; EBF = evergreen broadleaf forest; DNF = deciduous needleleaf forest; ENF = evergreen needleleaf forest; MIF = mixed forest; OSH = open shrubland; WET = wetland; BAR = barren lands.

4.3. Regional LE Estimation Based on MODIS-Derived SWIRs

4.3.1. Validation of the Estimated Regional Surface Fluxes

We compared the estimated regional R_n, G, LE_swir, and LE_no using daily gridded meteorological data with the ground measurements for all 25 sites. Table 5 illustrates the good agreement between the estimated daily R_n and G using gridded meteorological data versus the ground-measured flux measurements. The RMSE of the daily R_n for different biomes varies from 11.8 to 45.7 W/m^2, and the R^2 varies from 0.67 to 0.94 ($p < 0.01$). For the individual sites, the largest RMSE of 45.7 W/m^2 was observed for daily R_n, at the Xishuangbanna site. The errors in R_n may be caused by propagated errors from gridded R_s, $T_{\max}$, $T_{\min}$, e, albedo, EC ground-measured data, and discrepancies in spatial resolution. Similarly the R^2 of the estimated daily G using daily gridded meteorological data versus ground-measurements ranges from 0.41 to 0.63 ($p < 0.01$), and the RMSE ranges from 4.8 to 10.4 W/m^2 across all 25 flux tower sites. The biases in G may be mainly caused by the simple algorithm for G calculation that does not consider the differences among soil textures because of a lack of data

Table 5 also presents the statistical comparisons of the estimated daily LE (LE_swir and LE_no) using gridded meteorological data with the corresponding flux-tower measurements. The RMSE of the daily LE_swir (LE_no) for different biomes varies from 17.6 (20.2) to 59.7 (62.4) W/m^2, and the R^2 varies from 0.48 (0.44) to 0.80 (0.73; $p < 0.01$). When compared with the estimated LE (LE_swir and LE_no) values using tower meteorology, there was slightly worse agreement between the estimated daily LE (LE_swir and LE_no) using gridded meteorological data versus the ground measurements. However, for most flux tower sites, the LE_swir results still show 5% to 16.2% greater R^2 ($p < 0.01$) correspondence, as well as 3% to 15.6% lower RMSE differences compared with the ground-measured LE relative to the LE_sm results. Figure 6 demonstrates the ability of the two modified PT algorithms driven by gridded meteorological data to predict spatial variation in LE accurately. The RMSE of the site-averaged LE_swir estimates versus the ground-measured LE was 24.3 W/m^2 and R^2 was 0.74 ($p < 0.01$), and the LE_swir results were better than the LE_no results (RMSE = 26.7 W/m^2, R^2 = 0.69, $p < 0.01$). Overall, the estimated regional LE_swir and LE_no using daily gridded meteorological data displayed high accuracy according to the validation of daily and spatial variation in LE.

4.3.2. Regional LE Mapping From MODIS-Derived SWIRs

Figure 7 shows the spatial pattern of the estimated average daily LE_swir (2003–2005) in China. The LE results obtained by the algorithm were relatively higher in the CRO, WET, OSH, and forest areas in the north, northeast, central, and south regions of China. Lower LE values were found in the semiarid and arid GRA and BAR regions of Inner Mongolia, northwest China, and the Qinghai-Tibet regions of China. The LE_swir pattern was consistent with that obtained in previous studies (Y. Chen et al., 2014; Li et al., 2014; Yao et al., 2013). These results indicate that LE_swir can be used successfully to characterize the LE spatial patterns as well as the temporal dynamics corresponding to the climate and vegetation patterns.

Figure 8 shows the spatial pattern of the differences between LE_swir and LE_no as a percentage of LE_no (ΔLE), which indicates the regional impacts of water stress characterized by the MODIS-derived SWIRs on LE. Large terrestrial moisture constraints (ΔLE approximately up to −56%) mainly occurred in the semiarid and arid GRA and BAR regions of northwest China because SM is the dominant factor that limits the terrestrial LE (K. Wang & Dickinson, 2012). By contrast, the small terrestrial water constraints areas included CRO, WET, OSH, and forests regions in southeast China, where SM was not a main controlling factor in terms of LE. Overall, these results demonstrate that the terrestrial LE is strongly controlled by water supply constraints (ΔLE exceeding −30%) by more than 53% over China.

5. Discussion

5.1. Characterization of Water Constraints for Determining EF and LE Using MODIS-Derived SWIRs

The water supplies from both the soil and vegetation canopy are recognized as major constraints in the PT algorithms for the partition of H and LE under unsaturated soil and vegetation surfaces (Jin et al., 2011; Priestley & Taylor, 1972; K. Wang & Dickinson, 2012). Many previous studies have shown that MODIS-derived SWIRs are sensitive to SM and vegetation water when modeling LE (Daniela & Virginia, 2014; Huang et al., 2015; Olsen et al., 2015; Yebra et al., 2013). The f (sm)_swir and f (cm)_swir values used in this study effectively characterized the soil water availability and vegetation water information, respectively. Importantly, the good correlations between f (sm)_swir (and f (cm)_swir) and EF confirmed the sensitivity of the MODIS-derived SWIRs to the EF variability associated with variations in SM and LE (Table 3).

The point-observed SM used in this study to drive the PT algorithm for evaluating the ground-measured LE estimates might not be an effective variable for regional LE estimation because a single point may not adequately capture the spatial heterogeneity in SM at large scales (Wanders et al., 2012). Alternatively, the spatial resolution of the satellite-derived and reanalysis SM products may be too coarse to characterize heterogeneous SM conditions associated with the EF spatial heterogeneity at finer scales (Albergel et al., 2013; Dirmeyer et al., 2004; Miralles et al., 2011). Previous studies replaced SM with some key meteorological variables (e.g., Dongtan, RH, and VPD) in the PT model for estimating EFs. For instance, Granger and Gray (1989) combined the available surface energy ($R_n - G$) and drying power of the air to define a surface dryness index for simulating the terrestrial LE. K. Wang and Liang (2008) used the diurnal air temperature range as a surrogate for SM to investigate the effects of SM on LE. According to the complementary hypothesis of Bouchet (1963), the surface SM may be characterized by the atmospheric evaporative demand, while Fisher et al. (2008) directly defined RH^{VPD} as a soil water deficit index to constrain LE_s. However, using these soil evaporation parameters without considering the SM supply may lead to the overestimation of LE_s during extreme drought conditions (K. Wang et al., 2007; H. Yan et al., 2012). Fortunately, the f (sm)_swir parameter used in this study had relatively high spatial and temporal resolution, but it is also accounted for the effects of both the surface water supply and atmospheric evaporative demand on EF_s to improve the estimates of LE_s obtained from a combination of MODIS-derived SWIRs and RHD. The f (sm)_swir-based algorithm can effectively replace SM-based models, especially when there is a lack of SM data.

f (cm)_swir combines NDVI and LSWI to improve the sensitivity of vegetation water constraints to vegetation transpiration because the SWIR band in LSWI is more sensitive to the canopy water content than the red band used in NDVI, and together they can effectively reflect the internal water storage ability of woody plants to offset the SM demand (He et al., 2016; Reichstein et al., 2002; Wagle et al., 2014). By contrast, the ground-observed upper layer SM might not adequately represent the water constraints of deep-rooted vegetation because this vegetation can sustain elevated transpiration rates by extracting SM from deeply rooted

Table 5
Comparison of the Estimated daily R_n, G and LE (LE_swir and LE_no) Values Using Daily Gridded Meteorological Data With Corresponding Ground Measurements From All 25 Sites

		R_n			G			LE_swir			LE_no		
Name	IGBP	R^2	RMSE	bias	R^2	RMSE	bias	R^2	RMSE	bias	R^2	RMSE	bias
DX	CRO	0.81	28.4	−8.5	0.52	9.2	−4.7	0.57	42.4	−21.1	0.50	44.3	−20.3
GT	CRO	0.94	21.5	−4.1	0.45	8.9	−3.6	0.71	38.2	−15.5	0.65	40.4	−13.7
JZ	CRO	0.73	23.9	−4.6	0.52	7.5	−3.5	0.55	42.6	17.5	0.51	46.2	18.1
MY	CRO	0.89	35.2	−16.3	0.62	10.4	−7.3	0.76	33.3	12.3	0.71	38.5	13.2
TY	CRO	0.79	24.5	−7.7	0.41	9.5	−6.4	0.66	38.1	−6.8	0.61	42.3	−4.9
YC	CRO	0.93	25.9	10.8	0.51	9.8	3.2	0.75	26.9	−9.7	0.69	29.6	−8.8
AR	GRA	0.91	28.8	−4.9	0.45	5.7	−1.1	0.70	44.5	−27.5	0.64	48.3	−27.2
FK	GRA	0.70	27.4	14.5	0.48	7.6	4.4	0.48	37.1	11.2	0.44	40.9	14.5
NMG	GRA	0.81	22.7	9.8	0.60	5.5	2.6	0.65	26.3	−2.3	0.60	28.1	4.1
LZ	GRA	0.88	29.1	9.5	0.52	7.6	3.3	0.77	31.3	−16.6	0.71	35.4	−14.1
MQ	GRA	0.84	25.9	6.6	0.51	8.2	4.2	0.76	29.8	−17.4	0.72	32.3	−15.4
NQ	GRA	0.82	23.3	5.8	0.50	9.1	4.6	0.71	40.2	−24.9	0.67	43.5	−22.6
NaC	GRA	0.74	28.5	7.1	0.48	8.5	3.7	0.63	38.4	−20.3	0.57	41.6	−19.8
QY	GRA	0.90	29.4	13.1	0.55	7.5	1.1	0.78	45.1	−24.3	0.71	49.2	−23.3
HN	DBF	0.85	27.1	6.5	0.47	9.4	4.5	0.70	34.9	6.1	0.63	37.3	8.6
YY	DBF	0.83	22.6	7.8	0.44	7.8	3.5	0.65	36.8	7.9	0.60	39.1	8.5
DHS	EBF	0.89	23.5	4.2	0.49	6.2	3.8	0.78	30.3	2.8	0.68	33.7	3.9
XSBN	EBF	0.79	45.7	−12.9	0.46	4.8	2.1	0.58	48.6	−23.7	0.52	50.3	−22.2
LSH	DNF	0.82	37.4	2.6	0.45	8.2	3.1	0.67	32.5	−14.1	0.61	34.9	−13.6
QYZ	ENF	0.89	30.5	5.7	0.50	7.1	1.5	0.64	30.9	1.1	0.59	35.5	−2.4
CBS	MIF	0.91	22.8	7.2	0.53	9.1	3.5	0.69	42.2	−22.7	0.61	45.4	−21.8
HB	OSH	0.94	24.9	0.7	0.47	9.3	4.2	0.80	28.7	−17.2	0.73	30.3	−16.9
DT	WET	0.67	26.6	9.2	0.44	8.6	5.1	0.50	59.7	25.9	0.47	62.4	28.3
HZZ	BAR	0.75	33.2	−14.4	0.63	8.8	−3.3	0.57	22.9	9.5	0.49	25.8	11.2
SSW	BAR	0.87	11.8	−2.4	0.61	7.4	−4.8	0.69	17.6	−6.8	0.61	20.2	2.1

Note. All of the statistics were calculated at the 99% confidence level. Units for both RMSE and bias are all W/m^2. CRO = cropland; GRA = grassland; DBF = deciduous broadleaf forest; EBF = evergreen broadleaf forest; DNF = deciduous needleleaf forest; ENF = evergreen needleleaf forest; MIF = mixed forest; OSH = open shrubland; WET = wetland; BAR = barren lands; IGBP = International Geosphere-Biosphere Programme; LE = latent heat flux; RMSE = root-mean-squared error; IGBP = International Geosphere-Biosphere Programme.

systems (Juárez et al., 2007; K. Wang & Dickinson, 2012). This may explain why the *f* (cm)_swir results had higher correlations with the ground-observed EF compared with the *f* (cm)_no results at the forest flux tower sites.

The MODIS-derived SWIR metrics were also sensitive to other environmental constraint factors that influenced the soil and vegetation spectral reflectance values, including T_a, VPD, and f_{APAR}. In this study, both *f*

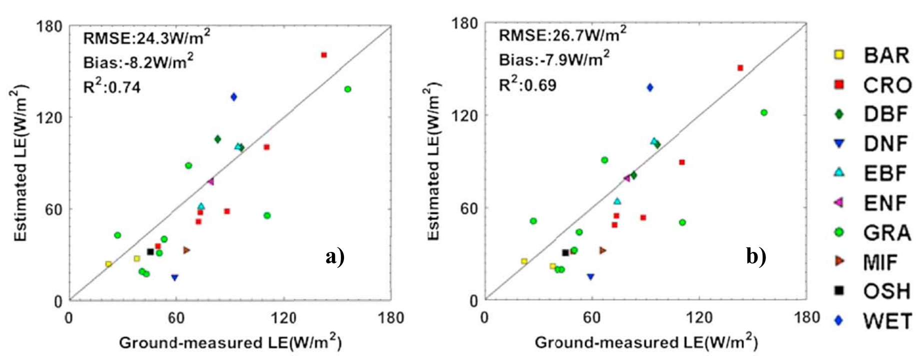

Figure 6. Comparisons of the estimated (a) LE_swir and (b) LE_no using daily gridded meteorological data and the corresponding measured site averaged daily LE values for different biomes at 25 sites. LE = latent heat flux; CRO = cropland; GRA = grassland; DBF = deciduous broadleaf forest; EBF = evergreen broadleaf forest; DNF = deciduous needleleaf forest; ENF = evergreen needleleaf forest; MIF = mixed forest; OSH = open shrubland; WET = wetland; BAR = barren lands.

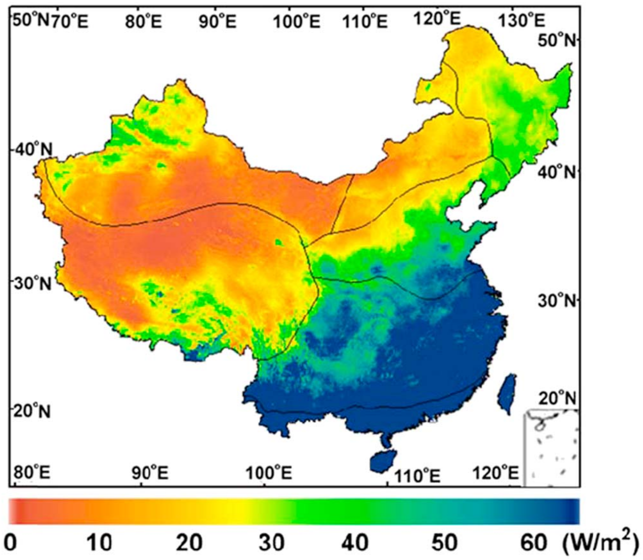

Figure 7. Spatial pattern of the estimated mean daily LE (2003–2005) in China using *f* (sm)_swir and *f* (cm)_swir as water supply constraints in the revised PT algorithm. Natural division boundaries are denoted by gray lines. LE = latent heat flux; PT = Priestley-Taylor.

(sm)_swir and *f* (cm)_swir were strongly positively correlated with T_a at the GRA sites ($R^2 > 0.45$) in the Inner Mongolia and Qinghai-Tibet regions, thereby indicating that the dynamics of the daily T_a was a dominant controlling factor that affected the variability of both *f* (sm)_swir and *f* (cm)_swir, while the associated cold T_a also induced variations in EF and LE for these biomes. However, we found no significant correlations between the MODIS-derived SWIR metrics and T_a at other biome sites where the cold T_a may have been less of a major constraint on LE than the low SM. The MODIS-derived SWIRs were correlated with VPD at the DBF and EBF sites ($R^2 > 0.41$), whereas they were not significantly correlated with VPD at the other biome sites. These results demonstrate that the MODIS-derived SWIRs were sensitive to SM-related impacts on the soil and vegetation reflectance values in addition to atmospheric VPD effects. *f* (cm)_swir was highly sensitive to plant structural and photosynthetic changes (indicated by f_{APAR}) at most of the biome sites ($R^2 > 0.54$). Other studies also demonstrated the potential utility of alternative MODIS-derived SWIRs as environmental stress indicators for simulating ET, GPP, and agricultural drought (Daniela & Virginia, 2014; Olsen et al., 2013; X. Xiao et al., 2004; Yebra et al., 2013; Y. Zhou et al., 2017). Thus, using alternative MODIS-derived SWIRs across multiple biomes may enhance the performance of the PT algorithm when estimating the regional LE under different environmental stress conditions.

5.2. Impacts of Water Stress on LE Using MODIS-Derived SWIRs

We highlighted the potential use of the MODIS-derived SWIRs as water supply indicators to characterize water (SM and vegetation canopy water content) constraints in the revised PT algorithm to estimate the terrestrial LE for a variety of land cover types throughout China. The estimated daily LE using the MODIS-derived SWIRs as a surrogate for water supply constraints was significantly better than LE_no at most of the flux tower sites. Similarly, LE_swir performed better than LE_sm at these flux tower sites. At the regional scale, the water stress impacts on LE determined using the MODIS-derived SWIRs were large in the semiarid and arid GRA and BAR regions of northwest China. In fact, the actual severity of the water stress areas could be larger than that indicated in Figure 8 due to land cover changes and agricultural irrigation by human activities, which may reduce the sensitivity of the MODIS-derived SWIRs to water supply deficits (He et al., 2016; W. Liu et al., 2018; Y. Zhou et al., 2017). These results indicate that the MODIS-derived SWIRs are sensitive proxies for water supply constraints when estimating the tower and regional LE values.

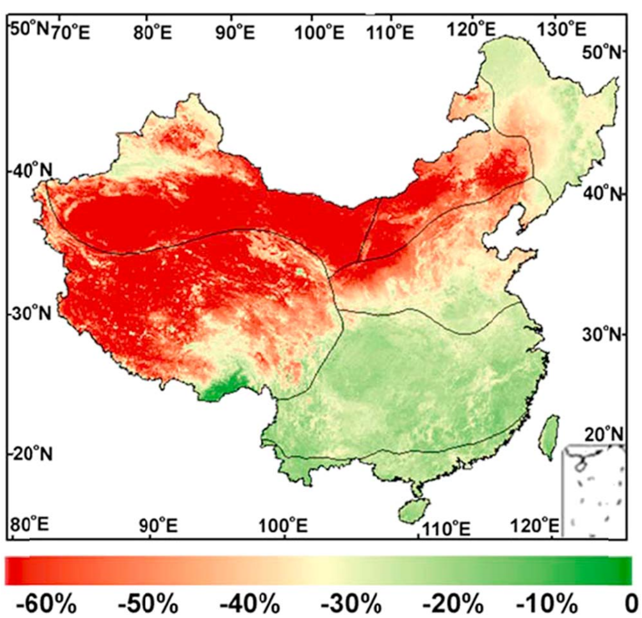

Figure 8. Spatial pattern of the estimated mean daily LE (2003–2005) difference percentage (ΔLE) in China between the estimated LE (LE_swir) using the MODIS-derived SWIRs and that (LE_no) without using SWIRs. Natural division boundaries are denoted by gray lines. LE = latent heat flux; SWIRs = shortwave infrared reflectance metrics; MODIS = MODerate-resolution Imaging Spectroradiometer.

The revised PT algorithm using MODIS-derived SWIRs exhibited a reliable and robust capacity for estimating the terrestrial LE, where the impacts of water stress on the estimations of EF and LE varied greatly among multiple biomes and climatic zones. For example, both *f* (sm)_swir and *f* (cm)_swir accounted for high amounts of the variability in the terrestrial EF for most of the CRO, GRA, DBF, DNF, MIF, OSH, and BAR flux tower sites (Table 3). Previous studies have demonstrated that MODIS-derived SWIRs respond strongly to the seasonal dynamics of the surface SM and vegetation water contents in the early stage of surface drought (Jackson et al., 2004; Maki et al., 2004; Olsen et al., 2015; Wagle et al., 2014; Yebra et al., 2013; Y. Zhou et al., 2017). The revised PT algorithm successfully captured the seasonal soil and vegetation cycles to improve the estimates of LE from the MODIS-derived SWIRs. By contrast, both *f* (sm)_swir and *f* (cm)_swir explained merely less than 24% of the variability in the terrestrial EF for the EBF, ENF, and WET flux tower sites. These biomes were located in subtropical humid climatic zones and were not water stressed, with weak seasonality in the SM and vegetation water contents, and the MODIS-derived SWIRs showed that the information loss and contamination over high reflectance areas were caused by the high cloud cover (Jackson et al., 2004; Sadeghi et al., 2017, 2015; Wagle et al., 2014; Y. Zhou et al., 2017). Consequently, the suitability of both *f* (sm)_swir and *f* (cm)_swir for reflecting variations in the SM and vegetation water contents was limited in these regions. X. Xiao et al. (2005) also found that the large seasonal cycles in the LSWI and Enhanced Vegetation Index values were caused by clouds when using the MODIS data from an ENF flux tower site at Howland, Maine, USA. Similarly, Daniela and Virginia (2014) proposed a simple index based on MODIS-derived SWIRs to represent the SM variations well at 15 CRO and GRA flux tower sites in the South Great Plains area, USA, and they also demonstrated that the modified PT algorithm optimized with this simple index only yields 11% errors in the ET. In addition, Huang et al. (2015) showed that integrating the MODIS-derived NDWI into the surface energy balance system as an indicator of water stress could avoid instantaneous overestimations of LE, where RMSE decreased by 33 W/m^2 at the irrigated CRO flux tower sites in the semiarid and arid regions of northwest China. These findings support our interpretations of the differences in the estimations of LE using MODIS-derived SWIRs as water stress factors for a variety of biomes.

5.3. Limitations and Future Research

A major issue according to the results of this investigation is the spatial scale mismatch between the footprints of EC measurements and MODIS-derived reflectance metric values (Baldocchi et al., 2001; Mu et al., 2011; Schmid, 1994; Yao et al., 2015). The typical EC flux tower footprints are about hundreds of meters depending on measurement height above canopy layer and WS (Baldocchi et al., 2001; Foken, 2008; K. Wang & Dickinson, 2012), which may be generally much smaller than the spatial resolution of the MODIS-derived reflectance products at 500 m. Thus, the MODIS-derived reflectance signals might not adequately reflect the subpixel scale SM and vegetation ecophysiological information at these EC flux tower sites, especially in complex and heterogeneous areas (Baldocchi, 2008; Yao et al., 2015; Zhang et al., 2010). Therefore, inaccurate MODIS-derived reflectance metrics representing the EC flux tower footprint may still introduce additional uncertainties into the estimates of LE.

A second source of uncertainty is the EC flux ground measurements and the associated surface energy imbalance problem due to the variations in wind patterns, the representation of the footprint, and the temporal sampling variability (Foken, 2008; Wilson et al., 2002). Currently, EC ground measurements provide the best reference data for evaluating satellite-based LE estimates. However, their typical measured errors are still 5–20% compared with the LE measurements obtained using other methods, such as the scintillometer method and sap flow technique, and their uncertainties still need to be interpreted (Mahrt, 2010; K. Wang & Dickinson, 2012). An important problem is that the averaged energy balance closure (R_e = (LE + H)/($R_n - G$)) for more than 60 flux tower sites provided by the FLUXNET project was approximately 0.8 (Wilson et al., 2002). It is possible that the EC method only accurately obtains small eddies, and it might not measure large eddies in the lower boundary layer, which may contribute to the energy imbalance (Foken, 2008; Franssen et al., 2010; Twine et al., 2000). In the present study, the LE measurements were corrected based on the method developed by Twine et al. (2000), but these corrections will still lead to substantial uncertainties in the EC ground-measured LE values, which were associated with evaluations of the impacts of water stress on LE.

Further studies are required to elucidate the parameterization of *f* (sm)_swir for different soil types over global vegetation and climate conditions to evaluate the impacts of water stress on LE because the *f* (sm)_swir parameter used in this study ignores the differences among soil types and textures. Other remote sensing data may provide additional water stress variables that influence the regional terrestrial LE, such as the hyperspectral remote sensing data (Oltra-Carrió et al., 2015), the terrestrial water storage changes acquired from Gravity Recovery and Climate Experiment measurements (Swenson & Wahr, 2002), and the downscaling SM data set from microwave remote sensing (Entekhabi et al., 2010; S. Gao et al., 2017). The MODIS-derived SWIRs are useful methods successfully quantifying the impacts of SM on terrestrial LE values because they are closer to the landscape scale, thereby potentially allowing the acquisition of finer spatial information regarding the impacts of heterogeneous soil and vegetation water stress.

6. Conclusion

In this study, we evaluated the impacts of moisture stress on terrestrial LE based on MODIS-derived SWIRs as water supply proxies for SM and vegetation water constraints in the revised PT model. In this revised PT algorithm, the SM constraint is parameterized by a combination of the SWIR SMI and an indicator of atmospheric evaporative demand (RHD), and the vegetation water constraint is optimized by NDVI and LSWI. This revised PT algorithm simultaneously considers the effects of the atmospheric evaporative demand and surface SM supply on LE_s. The estimated LE using the MODIS-derived SWIRs and that those without using SWIRs based on the revised PT algorithm were employed to assess the impacts on the terrestrial LE of SWIRs related to the water supply.

Evaluations conducted at 25 EC flux tower sites in China indicated that the revised PT algorithm based on the MODIS-derived SWIRs could be used to effectively estimate the terrestrial LE accurately. The sensitivity analysis results suggested that the MODIS-derived SWIRs were sensitive to variations in SM and plant water. The use of MODIS-derived SWIRs as water supply constraints in the revised PT algorithm improved the algorithm's performance compared with alternative LE estimation methods using the ground-measured SM inputs (LE_sm) or without SWIRs based on the water supply constraint (LE_no) for most of the flux tower sites representing different land cover types. Regional model analysis using the MODIS-derived SWIRs as water supply proxies indicated that water restrictions limited the terrestrial LE by more than 53% over China, particularly in the drier climate areas of northwest China where atmospheric VPD and RH were not sufficient to characterize both the atmospheric demand and water supply.

Acknowledgments
We thank both Ziwei Xu and Tongren Xu from Faculty of Geographical Science, Beijing Normal University, China, for their suggestions to improve this manuscript. We also thank the International Science Editing (http://www.internationalscienceediting.com) for editing this manuscript. All the data used are listed in the references. This work was partially supported by the Natural Science Fund of China (41671331) and the National Key Research and Development Program of China (2016YFA0600102 and 2016YFB0501404). J. B. F. contributed to this paper from the Jet Propulsion Laboratory, California Institute of Technology, under a contract with the National Aeronautics and Space Administration. California Institute of Technology. Government sponsorship acknowledged. J. B. F. was supported in part by *NASA SUSMAP*.

References

Albergel, C., Dorigo, W., Reichle, R. H., Balsamo, G., de Rosnay, P., Muñoz-Sabater, J., et al. (2013). Skill and global trend analysis of soil moisture from reanalyses and microwave remote sensing. *Journal of Hydrometeorology*, *14*(4), 1259–1277. https://doi.org/10.1175/JHM-D-12-0161.1

Allen, R. G., Pereira, L. S., Raes, D., & Smith, M. (1998). Crop evapotranspiration: Guidelines for computing crop requirements, FAO irrigation and drainage paper 56, Food and Agricultural Organization of the U.N., Rome.

Baldocchi, D. (2008). Breathing of the terrestrial biosphere: Lessons learned from a global network of carbon dioxide flux measurement systems. *Australian Journal of Botany*, *56*(1), 1–26. https://doi.org/10.1071/BT07151

Baldocchi, D., Falge, E., Gu, L., Olson, R., Hollinger, D., Running, S., et al. (2001). FLUXNET: A new tool to study the temporal and spatial variability of ecosystem-scale carbon dioxide, water vapor, and energy flux densities. *Bulletin of the American Meteorological Society*, *82*(11), 2415–2434. https://doi.org/10.1175/1520-0477(2001)082<2415:FANTTS>2.3.CO;2

Barton, C. V. M., & North, P. R. J. (2001). Remote sensing of light use efficiency using the photochemical reflectance index: Model and sensitivity analysis. *Remote Sensing of Environment*, *78*(3), 264–273. https://doi.org/10.1016/S0034-4257(01)00224-3

Bouchet, R. J. (1963). Evapotranspiration re'elle evapotranspiration potentielle, signification climatique. *Int. Assoc. Sci. Hydrol.*, *2*, 134–142.

Carlson, T., & Ripley, D. (1997). On the relation between NDVI, fractional vegetation cover, and leaf area index. *Remote Sensing of Environment*, *62*(3), 241–252. https://doi.org/10.1016/S0034-4257(97)00104-1

Ceccato, P., Flasse, S., Tarantola, S., Jacquemoud, S., & Grégoire, J. M. (2001). Detecting vegetation leaf water content using reflectance in the optical domain. *Remote Sensing of Environment*, *77*(1), 22–33. https://doi.org/10.1016/S0034-4257(01)00191-2

Chen, D., Huang, J., & Jackson, T. (2005). Vegetation water content estimation for corn and soybeans using spectral indices derived from MODIS near- and short-wave infrared bands. *Remote Sensing of Environment*, *98*(2-3), 225–236. https://doi.org/10.1016/j.rse.2005.07.008

Chen, Y., Xia, J., Liang, S., Feng, J., Fisher, J. B., Li, X., et al. (2014). Comparison of satellite based evapotranspiration models over terrestrial ecosystems in China. *Remote Sensing of Environment*, *140*, 279–293.

Chen, Y., Yang, K., He, J., Qin, J., Shi, J., du, J., & He, Q. (2011). Improving land surface temperature modeling for dry land of China. *Journal of Geophysical Research*, *116*, D20104. https://doi.org/10.1029/2011JD015921

Daniela, G., & Virginia, V. (2014). Evapotranspiration and water stress estimation from TIR and SWIR bands. *Agriculture, Forestry and Fisheries*, *3*, 36–45.

Dirmeyer, P. A., Guo, Z., & Gao, X. (2004). Comparison, validation and transferability of eight multi-year global soil wetness products. *Journal of Hydrometeorology*, *5*(6), 1011–1033. https://doi.org/10.1175/JHM-388.1

Entekhabi, D., Njoku, E. G., O'Neill, P. E., Kellogg, K. H., Crow, W. T., Edelstein, W. N., et al. (2010). The soil moisture active passive (SMAP) mission. *Proc. IEEE.*, *98*(5), 704–716. https://doi.org/10.1109/JPROC.2010.2043918

Fernández, R., Montes, H., & Salinas, C. (2015). VIS-NIR, SWIR and LWIR imagery for estimation of ground bearing capacity. *Sensors*, *15*(6), 13,994–14,015. https://doi.org/10.3390/s150613994

Fisher, J. B., Melton, F., Middleton, E., Hain, C., Anderson, M., Allen, R., et al. (2017). The Future of Evapotranspiration: Global requirements for ecosystem functioning, carbon and climate feedbacks, agricultural management, and water resources. *Water Resources Research*, *53*, 2618–2626. https://doi.org/10.1002/2016WR020175

Fisher, J. B., Tu, K. P., & Baldocchi, D. D. (2008). Global estimates of the land atmosphere water flux based on monthly AVHRR and ISLSCP-II data, validated at 16 FLUXNET sites. *Remote Sensing of Environment*, *112*(3), 901–919. https://doi.org/10.1016/j.rse.2007.06.025

Foken, T. (2008). The energy balance closure problem: An overview. *Ecological Applications*, *18*(6), 1351–1367. https://doi.org/10.1890/06-0922.1

Franssen, H. J. H., Stöckli, R., Lehner, L., Rotenberg, E., & Seneviratne, S. I. (2010). Energy balance closure of eddy-covariance data: A multisite analysis for European FLUXNET stations. *Agricultural and Forest Meteorology*, *150*(12), 1553–1567. https://doi.org/10.1016/j.agrformet.2010.08.005

Friedl, M., McIver, D. K., Hodges, J. C. F., Zhang, X. Y., Muchoney, D., Strahler, A. H., et al. (2002). Global land cover mapping from MODIS: Algorithms and early results. *Remote Sensing of Environment*, *83*(1-2), 287–302. https://doi.org/10.1016/S0034-4257(02)00078-0

Fu, Y. L., Yu, G. R., Sun, X. M., Li, Y. N., Wen, X. F., Zhang, L. M., et al. (2006). Depression of net ecosystem CO_2 exchange in semi-arid *Leymus chinensis* steppe and alpine shrub. *Agricultural and Forest Meteorology*, *137*(3-4), 234–244. https://doi.org/10.1016/j.agrformet.2006.02.009

Gao, B. (1996). NDWI: A normalized difference water index for remote sensing of vegetation liquid water from space. *Remote Sensing of Environment*, *58*(3), 257–266. https://doi.org/10.1016/S0034-4257(96)00067-3

Gao, S., Zhu, Z., & Weng, H. (2017). Upscaling of sparse in situ soil moisture observations by integrating auxiliary information from remote sensing. *International Journal of Remote Sensing*, *38*(17), 4782–4803. https://doi.org/10.1080/01431161.2017.1320444

Garcia, M., Sandholt, I., Ceccato, P., Ridler, M., Mougin, E., Kergoat, L., et al. (2013). Actual evapotranspiration in drylands derived from in-situ and satellite data: Assessing biophysical constraints. *Remote Sensing of Environment*, *131*, 103–118. https://doi.org/10.1016/j.rse.2012.12.016

Goerner, A., Reichstein, M., Tomelleri, E., Hanan, N., Rambal, S., Papale, D., et al. (2011). Remote sensing of ecosystem light use efficiency with MODIS based PRI. *Biogeosciences*, *8*(1), 189–202. https://doi.org/10.5194/bg-8-189-2011

Granger, R. J., & Gray, D. M. (1989). Evaporation from natural nonsaturated surfaces. *Journal of Hydrology*, *111*(1-4), 21–29. https://doi.org/10.1016/0022-1694(89)90249-7

Guan, D. X., Wu, J. B., Zhao, X. S., Han, S. J., Yu, G. R., Sun, X. M., & Jin, C. J. (2006). CO_2 fluxes over an old temperate mixed forest in northeastern China. *Agricultural and Forest Meteorology*, *137*(3-4), 138–149. https://doi.org/10.1016/j.agrformet.2006.02.003

Hao, X. C., Zhang, Q., & Yang, Z. S. (2016). A new index for land surface in homogeneity and its impact on sensible heat flux measured by Large Aperture Scintillometer (LAS) over eastern Gansu of Loess plateau (in Chinese). *Chinese Journal of Geophysics*, *59*, 816–827.

He, J., & Yang, K. (2011). China meteorological forcing dataset; *cold and arid regions science data center: Lanzhou, China*. https://doi.org/10.3972/westdc.002.2014.db

He, M., Kimball, J. S., Running, S., Ballantyne, A., Guan, K., & Huemmrich, F. (2016). Satellite detection of soil moisture related water stress impacts on ecosystem productivity using the MODIS-based photochemical reflectance index. *Remote Sensing of Environment*, *186*, 173–183. https://doi.org/10.1016/j.rse.2016.08.019

He, W., & Kobayashi, T. (1998). A rational parameterization of evaporation from dry, bare soil. *Journal of the Meteorological Society of Japan*, *76*(6), 955–963. https://doi.org/10.2151/jmsj1965.76.6_955

Huang, C., Li, Y., Gu, J., Lu, L., & Li, X. (2015). Improving estimation of evapotranspiration under water-limited conditions based on SEBS and MODIS data in arid regions. *Remote Sensing*, *7*(12), 16,795–16,814. https://doi.org/10.3390/rs71215854

Jackson, T. J., Chen, D., Cosh, M., Li, F., Anderson, M., Walthall, C., et al. (2004). Vegetation water content mapping using Landsat data derived normalized difference water index for corn and soybeans. *Remote Sensing of Environment*, *92*(4), 475–482. https://doi.org/10.1016/j.rse.2003.10.021

Jia, Z., Liu, S., Xu, Z., Chen, Y., & Zhu, M. (2012). Validation of remotely sensed evapotranspiration over the Hai River basin, China. *Journal of Geophysical Research*, *117*, D13113. https://doi.org/10.1029/2011JD017037

Jiang, L., & Islam, S. (2001). Estimation of surface evaporation map over southern Great Plains using remote sensing data. *Water Resources Research*, *37*, 329–340. https://doi.org/10.1029/2000WR900255

Jin, Y., Randerson, J., & Goulden, M. (2011). Continental-scale net radiation and evapotranspiration estimated using MODIS satellite observations. *Remote Sensing of Environment*, *115*(9), 2302–2319. https://doi.org/10.1016/j.rse.2011.04.031

Juárez, R. I. N., Hodnett, M. G., Fu, R., Goulden, M. L., & von Randow, C. (2007). Control of dry season evapotranspiration over the Amazonian forest as inferred from observations at a southern Amazon forest site. *Journal of Climate*, *20*(12), 2827–2839. https://doi.org/10.1175/JCLI4184.1

Jung, M., Reichstein, M., Ciais, P., Seneviratne, S. I., Sheffield, J., Goulden, M. L., et al. (2010). Recent decline in the global land evapotranspiration trend due to limited moisture supply. *Nature*, *467*(7318), 951–954. https://doi.org/10.1038/nature09396

Kalma, J., McVicar, T., & McCabe, M. (2008). Estimating land surface evaporation: A review of methods using remotely sensed surface temperature data. *Surveys in Geophysics*, *29*(4-5), 421–469. https://doi.org/10.1007/s10712-008-9037-z

Li, M., Babel, W., Chen, X., Zhang, L., Sun, F., Wang, B., et al. (2015). A 3-year dataset of sensible and latent heat fluxes from the Tibetan plateau, derived using eddy covariance measurements. *Theoretical and Applied Climatology*, *122*(3-4), 457–469. https://doi.org/10.1007/s00704-014-1302-0

Li, X., Cheng, G., Liu, S., Xiao, Q., Ma, M., Jin, R., et al. (2013). Heihe watershed allied telemetry experimental research (HiWATER): Scientific objectives and experimental design. *Bulletin of the American Meteorological Society*, *94*(8), 1145–1160. https://doi.org/10.1175/BAMS-D-12-00154.1

Li, X., Liang, S., Yuan, W., Yu, G., Cheng, X., Chen, Y., et al. (2014). Estimation of evapotranspiration over the terrestrial ecosystems in China. *Ecohydrology*, *7*(1), 139–149. https://doi.org/10.1002/eco.1341

Liu, R., Pan, L. P., Jenerette, G. D., Wang, Q. X., Cieraad, E., & Li, Y. (2012). High efficiency in water use and carbon gain in a wet year for a desert halophyte community. *Agricultural and Forest Meteorology*, *162-163*, 127–135. https://doi.org/10.1016/j.agrformet.2012.04.015

Liu, S., Xu, Z., Zhu, Z., Jia, Z., & Zhu, M. (2013). Measurements of evapotranspiration from eddy-covariance systems and large aperture scintillometers in the Hai River basin, China. *Journal of Hydrology*, *487*, 24–38. https://doi.org/10.1016/j.jhydrol.2013.02.025

Liu, S., Xu, Z. W., Wang, W. Z., Jia, Z. Z., Zhu, M. J., et al. (2011). A comparison of eddy covariance and large aperture scintillometer measurements with respect to the energy balance closure problem. *Hydrology and Earth System Sciences*, *15*(4), 1291–1306. https://doi.org/10.5194/hess-15-1291-2011

Liu, W., Dong, J., Xiang, K., Wang, S., Han, W., & Yuan, W. (2018). A sub-pixel method for estimating planting fraction of paddy rice in northeast China. *Remote Sensing of Environment*, *205*, 305–314. https://doi.org/10.1016/j.rse.2017.12.001

Liu, X., & Liu, J. (2014). Using short wave visible-near infrared reflectance spectroscopy to predict soil properties and content. *Spectroscopy Letters*, *47*, 729–739.

Long, D., & Singh, V. P. (2012). A two-source trapezoid model for evapotranspiration (TTME) from satellite imagery. *Remote Sens. Environ.*, *121*, 370–388. https://doi.org/10.1016/j.rse.2012.02.015

Lu, X., & Zhuang, Q. (2010). Evaluating evapotranspiration and water-use efficiency of terrestrial ecosystems in the conterminous United States using MODIS and AmeriFlux data. *Remote Sensing of Environment*, *114*(9), 1924–1939. https://doi.org/10.1016/j.rse.2010.04.001

Lucht, W., Schaaf, C. B., & Strahler, A. H. (2000). An algorithm for the retrieval of albedo from space using semiempirical BRDF models. *IEEE Transactions on Geoscience and Remote Sensing*, *38*(2), 977–998. https://doi.org/10.1109/36.841980

Ma, Y., Zhu, Z., Zhong, L., Wang, B., Han, C., Wang, Z., et al. (2014). Combining MODIS, AVHRR and in situ data for evapotranspiration estimation over heterogeneous landscape of the Tibetan plateau. *Atmospheric Chemistry and Physics*, *14*(3), 1507–1515. https://doi.org/10.5194/acp-14-1507-2014

Mahrt, L. (2010). Computing turbulent fluxes near the surface: Needed improvements. *Agricultural and Forest Meteorology*, *150*(4), 501–509. https://doi.org/10.1016/j.agrformet.2010.01.015

Maki, M., Ishiahra, M., & Tamura, M. (2004). Estimation of leaf water status to monitor the risk of forest fires by using remotely sensed data. *Remote Sensing of Environment*, *90*(4), 441–450. https://doi.org/10.1016/j.rse.2004.02.002

Miralles, D., Holmes, T. R. H., de Jeu, R. A. M., Gash, J. H., Meesters, A. G. C. A., & Dolman, A. J. (2011). Global land-surface evaporation estimated from satellite-based observations. *Hydrology and Earth System Sciences*, *15*(2), 453–469. https://doi.org/10.5194/hess-15-453-2011

Monteith, J. (1965). Evaporation and environment. *Symposia of the Society for Experimental Biology*, *19*, 205–224.

Morillas, L., Leuning, R., Villagarcía, L., García, M., Serrano-Ortiz, P., & Domingo, F. (2013). Improving evapotranspiration estimates in Mediterranean drylands: The role of soil evaporation. *Water Resources Research*, *49*, 6572–6586. https://doi.org/10.1002/wrcr.20468

Mu, Q., Heinsch, F., Zhao, M., & Running, S. (2007). Development of a global evapotranspiration algorithm based on MODIS and global meteorology data. *Remote Sensing of Environment*, *111*(4), 519–536. https://doi.org/10.1016/j.rse.2007.04.015

Mu, Q., Zhao, M., & Running, S. (2011). Improvements to a MODIS global terrestrial evapotranspiration algorithm. *Remote Sensing of Environment*, *115*(8), 1781–1800. https://doi.org/10.1016/j.rse.2011.02.019

Olsen, J., Ceccato, P., Proud, S., Fensholt, R., Grippa, M., Mougin, E., et al. (2013). Relation between seasonally detrended shortwave infrared reflectance data and land surface moisture in semi-arid Sahel. *Remote Sensing*, *5*(6), 2898–2927. https://doi.org/10.3390/rs5062898

Olsen, J., Stisen, S., Proud, S., & Fensholt, R. (2015). Evaluating EO-based canopy water stress from seasonally detrended NDVI and SIWSI with modeled evapotranspiration in the Senegal River basin. *Remote Sensing of Environment*, *159*, 57–69. https://doi.org/10.1016/j.rse.2014.11.029

Oltra-Carrió, R., Baup, F., Fabre, S., Fieuzal, R., & Briottet, X. (2015). Improvement of soil moisture retrieval from hyperspectral VNIR-SWIR data using clay content information: From laboratory to field experiments. *Remote Sensing*, *7*(3), 3184–3205. https://doi.org/10.3390/rs70303184

Priestley, C. H. B., & Taylor, R. J. (1972). On the assessment of surface heat flux and evaporation using large-scale parameters. *Monthly Weather Review*, *100*(2), 81–92. https://doi.org/10.1175/1520-0493(1972)100<0081:OTAOSH>2.3.CO;2

Reichstein, M., Tenhunen, J. D., Roupsard, O., Ourcival, J.-M., Rambal, S., Miglietta, F., et al. (2002). Severe drought effects on ecosystem CO_2 and H_2O fluxes at three Mediterranean evergreen sites: Revision of current hypotheses? *Global Change Biology*, *8*, 1365–2486.

Sadeghi, M., Babaeian, E., Tuller, M., & Jones, S. B. (2017). The optical trapezoid model: A novel approach to remote sensing of soil moisture applied to Sentinel-2 and Landsat-8 observations. *Remote Sensing of Environment*, *198*, 52–68. https://doi.org/10.1016/j.rse.2017.05.041

Sadeghi, M., Jones, S., & Philpot, W. (2015). A linear physically-based model for remote sensing of soil moisture using short wave infrared bands. *Remote Sensing of Environment*, *164*, 66–76. https://doi.org/10.1016/j.rse.2015.04.007

Schimel, D., Pavlick, R., Fisher, J. B., Asner, G. P., Saatchi, S., Townsend, P., et al. (2014). Observing terrestrial ecosystems and the carbon cycle from space. *Global Change Biology*, *21*, 1762–1776.

Schmid, H. P. (1994). Source areas for scalars and scalar fluxes. *Boundary-Layer Meteorology*, *67*(3), 293–318. https://doi.org/10.1007/BF00713146

Sun, X. M., Zhu, Z. L., Wen, X. F., Yuan, G. F., & Yu, G. R. (2006). The impact of averaging periods on eddy fluxes observed at ChinaFLUX sites. *Agricultural and Forest Meteorology*, *137*(3-4), 188–193. https://doi.org/10.1016/j.agrformet.2006.02.012

Swenson, S., & Wahr, J. (2002). Methods for inferring regional surface-mass anomalies from Gravity Recovery and Climate Experiment (GRACE) measurements of time-variable gravity. *Journal of Geophysical Research*, *107*(B9), 2193. https://doi.org/10.1029/2001JB000576

Twine, T. E., Kustas, W. P., Norman, J. M., Cook, D. R., Houser, P. R., Meyers, T. P., et al. (2000). Correcting eddy covariance flux underestimates over a grassland. *Agricultural and Forest Meteorology*, *103*(3), 279–300. https://doi.org/10.1016/S0168-1923(00)00123-4

Wagle, P., Xiao, X., Torn, M., Cook, D., Matamala, R., Fischer, M., et al. (2014). Sensitivity of vegetation indices and gross primary production of tallgrass prairie to severe drought. *Remote Sensing of Environment*, *152*, 1–14.

Wanders, N., Karssenberg, D., Bierkens, M., Parinussa, R., de Jeu, R., van Dam, J., & de Jong, S. (2012). Observation uncertainty of satellite soil moisture products determined with physically-based modeling. *Remote Sensing of Environment*, *127*, 341–356. https://doi.org/10.1016/j.rse.2012.09.004

Wang, H., Jia, G., Fu, C., Feng, J., Zhao, T., & Ma, Z. (2010). Deriving maximal light use efficiency from coordinated flux measurements and satellite data for regional gross primary production modeling. *Remote Sensing of Environment*, *114*(10), 2248–2258. https://doi.org/10.1016/j.rse.2010.05.001

Wang, H., Saigusa, N., Zu, Y., Wang, W., Yamamoto, S., & Kondo, H. (2008). Carbon fluxes and their responses to environmental variables in a Dahurian larch forest ecosystem in northeast China. *Journal of Forestry Research*, *19*(1), 1–10. https://doi.org/10.1007/s11676-008-0001-z

Wang, K., & Dickinson, R. (2012). A review of global terrestrial evapotranspiration: Observation, modeling, climatology, and climatic variability. *Reviews of Geophysics*, *50*, RG2005. https://doi.org/10.1029/2011RG000373

Wang, K., Dickinson, R., Wild, M., & Liang, S. (2010). Evidence for decadal variation in global terrestrial evapotranspiration between 1982 and 2002: 1. Model development. *Journal of Geophysical Research*, *115*, D20112. https://doi.org/10.1029/2009JD013671

Wang, K., & Liang, S. (2008). An improved method for estimating global evapotranspiration based on satellite determination of surface net radiation, vegetation index, temperature, and soil moisture. *Journal of Hydrometeorology*, *9*(4), 712–727. https://doi.org/10.1175/2007JHM911.1

Wang, K., Wang, P., Li, Z., Sparrow, M., & Cribb, M. (2007). A simple method to estimate evapotranspiration from a combination of net radiation, vegetation indices and temperatures. *Journal of Geophysical Research*, *112*, D15107. https://doi.org/10.1029/2006JD008351

Wang, X. F., Ma, M., Huang, G., Veroustraete, F., Zhang, Z., Song, Y., & Tan, J. (2012). Vegetation primary production estimation at maize and alpine meadow over the Heihe River basin, China. *International Journal of Applied Earth Observation and Geoinformation*, *17*, 94–101. https://doi.org/10.1016/j.jag.2011.09.009

Wang, Z. S., Schaaf, C. B., Sun, Q. S., Shuai, Y. M., & Román, M. O. (2018). Capturing rapid land surface dynamics with Collection V006 MODIS BRDF/NBAR/albedo (MCD43) products. *Remote Sensing of Environment*, *207*, 50–64. https://doi.org/10.1016/j.rse.2018.02.001

Wei, Y., Shenghua, G., Xudong, Z., Shaobo, G., Xiaosong, Z., Zeping, J., & Yunlong, W. (2012). Source area in-FLUX measurements by FSAM model over the *Populus deltoides* plantation in Yueyang (in Chinese). *Scientia Silvae Sinicae*, *48*, 16–21.

Wen, X. F., Yu, G. R., Sun, X. M., Li, Q. K., Liu, Y. F., Zhang, L. M., et al. (2006). Soil moisture effects on the temperature dependence of ecosystem respiration in a subtropical Pinus plantation of southern China. *Agricultural and Forest Meteorology*, *137*(3-4), 166–175. https://doi.org/10.1016/j.agrformet.2006.02.005

Wilson, K., Goldstein, A., Falge, E., Aubinet, M., Baldocchi, D., Berbigier, P., et al. (2002). Energy balance closure at FLUXNET sites. *Agricultural and Forest Meteorology*, *113*(1-4), 223–243. https://doi.org/10.1016/S0168-1923(02)00109-0

Wu, C., Niu, Z., & Gao, S. (2010). Gross primary production estimation from MODIS data with vegetation index and photosynthetically active radiation in maize. *Journal of Geophysical Research*, *115*, D12127. https://doi.org/10.1029/2009JD013023

Xiao, J., Zhuang, Q., Law, B. E., Chen, J., Baldocchi, D. D., Cook, D. R., et al. (2010). A continuous measure of gross primary production for the conterminous United States derived from MODIS and AmeriFlux data. *Remote Sensing of Environment*, *114*(3), 576–591. https://doi.org/10.1016/j.rse.2009.10.013

Xiao, X., Boles, S., Frolking, S., Salas, W., Moore, B. III, Li, C., et al. (2002). Observation of flooding and rice transplanting of paddy rice fields at the site to landscape scales in China using VEGETATION sensor data. *International Journal of Remote Sensing*, *23*(15), 3009–3022. https://doi.org/10.1080/01431160110107734

Xiao, X., Hollinger, D., Aber, J., Goltz, M., Davidson, E. A., Zhang, Q., & Moore, B. III (2004). Satellite-based modeling of gross primary production in an evergreen needleleaf forest. *Remote Sensing of Environment*, *89*(4), 519–534. https://doi.org/10.1016/j.rse.2003.11.008

Xiao, X., Zhang, Q., Hollinger, D., Aber, J., & Moore, B. III (2005). Modeling gross primary production of an evergreen needleleaf forest using MODIS and climate data. *Ecological Applications*, *15*(3), 954–969. https://doi.org/10.1890/04-0470

Xu, T., Bateni, S. M., Margulis, S. A., Song, L., Liu, S., & Xu, Z. (2016). Partitioning evapotranspiration into soil evaporation and canopy transpiration via a two source variational data assimilation system. *Journal of Hydrometeorology*, *17*, 2363–2370.

Xu, T., Liu, S., Liang, S., & Qin, J. (2011). Improving predictions of water and heat fluxes by assimilating MODIS land surface temperature products into common land model. *Journal of Hydrometeorology*, *12*(2), 227–244. https://doi.org/10.1175/2010JHM1300.1

Xu, Z., Liu, S., Li, X., Shi, S., Wang, J., Zhu, Z., et al. (2013). Intercomparison of surface energy flux measurement systems used during the HiWATER-MUSOEXE. *Journal of Geophysical Research: Atmospheres*, *118*, 13,140–13,157. https://doi.org/10.1002/2013JD020260

Yan, H., Wang, S. Q., Billesbach, D., Oechel, W., Zhang, J. H., Meyers, T., et al. (2012). Global estimation of evapotranspiration using a leaf area index-based surface energy and water balance model. *Remote Sensing of Environment*, *124*, 581–595. https://doi.org/10.1016/j.rse.2012.06.004

Yan, Y., Zhao, B., Chen, J. Q., Guo, H. Q., Gu, Y. J., Wu, Q. H., & Li, B. (2008). Closing the carbon budget of estuarine wetlands with tower-based measurements and MODIS time series. *Global Change Biology*, *14*(7), 1690–1702. https://doi.org/10.1111/j.1365-2486.2008.01589.x

Yang, K., He, J., Tang, W., Qin, J., & Cheng, C. (2010). On downward shortwave and longwave radiations over high altitude regions: Observation and modeling in the Tibetan plateau. *Agricultural and Forest Meteorology*, *150*(1), 38–46. https://doi.org/10.1016/j.agrformet.2009.08.004

Yang, Y., & Shang, S. (2013). A hybrid dual-source scheme and trapezoid framework-based evapotranspiration model (HTEM) using satellite images: Algorithm and model test. *Journal of Geophysical Research: Atmospheres*, *118*, 2284–2300. https://doi.org/10.1002/jgrd.50259

Yao, Y., Liang, S., Cheng, J., Liu, S., Fisher, J. B., Zhang, X., et al. (2013). MODIS-driven estimation of terrestrial latent heat flux in China based on a modified Priestley-Taylor algorithm. *Agricultural and Forest Meteorology*, *171-172*, 187–202. https://doi.org/10.1016/j.agrformet.2012.11.016

Yao, Y., Liang, S., Yu, J., Chen, J., Liu, S., Lin, Y., et al. (2017). A simple temperature domain two-source model for estimating agricultural field surface energy fluxes from Landsat images. *Journal of Geophysical Research: Atmospheres*, *122*, 5211–5236. https://doi.org/10.1002/2016JD026370

Yao, Y., Liang, S., Li, X., Chen, J., Wang, K., Jia, K., et al. (2015). A satellite-based hybrid algorithm to determine the Priestley-Taylor parameter for global terrestrial latent heat flux estimation across multiple biomes. *Remote Sensing of Environment*, *165*, 216–233.

Yao, Y., Liang, S., Li, X., Hong, Y., Fisher, J. B., Zhang, N., et al. (2014). Bayesian multimodel estimation of global terrestrial latent heat flux from eddy covariance, meteorological, and satellite observations. *Journal of Geophysical Research: Atmospheres*, *119*, 4521–4545. https://doi.org/10.1002/2013JD020864

Yebra, M., Van Dijk, A., Leuning, R., Huete, A., & Guerschman, J. (2013). Evaluation of optical remote sensing to estimate actual evapotranspiration and canopy conductance. *Remote Sensing of Environment*, *129*, 250–261. https://doi.org/10.1016/j.rse.2012.11.004

Yilmaz, M. T., Hunt, E. R. Jr., & Jackson, T. J. (2008). Remote sensing of vegetation water content from equivalent water thickness using satellite imagery. *Remote Sensing of Environment*, *112*(5), 2514–2522. https://doi.org/10.1016/j.rse.2007.11.014

Yu, G., Wen, X., Sun, X., Tanner, B., Lee, X., & Chen, J. (2006). Overview of ChinaFLUX and evaluation of its eddy covariance measurement. *Agricultural and Forest Meteorology*, *137*(3-4), 125–137. https://doi.org/10.1016/j.agrformet.2006.02.011

Yuan, Y., Liu, S., Yu, G., Bonnefond, J.-M., Chen, J., Davis, K., et al. (2010). Global estimates of evapotranspiration and gross primary production based on MODIS and global meteorology data. *Remote Sensing of Environment*, *114*(7), 1416–1431. https://doi.org/10.1016/j.rse.2010.01.022

Zarco-Tejada, P. J., Rueda, C. A., & Ustin, S. L. (2003). Water content estimation in vegetation with MODIS reflectance data and model inversion methods. *Remote Sensing of Environment*, *85*(1), 109–124. https://doi.org/10.1016/S0034-4257(02)00197-9

Zhang, F., & Zhou, G. Y. (2017). Deriving a light use efficiency estimation algorithm using in situ hyperspectral and eddy covariance measurements for a maize canopy in northeast China. *Ecology and Evolution*, *7*(13), 4735–4744. https://doi.org/10.1002/ece3.3051

Zhang, K., Kimball, J., Nemani, R., & Running, S. (2010). A continuous satellite-derived global record of land surface evapotranspiration from 1983 to 2006. *Water Resources Research*, *46*, W09522. https://doi.org/10.1029/2009WR008800

Zhang, Q. (1998). Determination and application of drought index in north China (in Chinese). *Journal of Catastrophology*, *13*, 34–38.

Zhang, R., Sun, X., Wang, W., Xu, J., Zhu, Z., & Tian, J. (2005). An operational two-layer remote sensing model to estimate surface flux in regional scale: Physical background. *Science in China, Series D: Earth Sciences*, *48*, 225–244.

Zhou, G. Y., Wei, X., Wu, Y., Liu, S., Huang, Y., Yan, J., et al. (2011). Quantifying the hydrological responses to climate change in an intact forested small watershed in southern China. *Global Change Biology*, *17*(12), 3736–3746. https://doi.org/10.1111/j.1365-2486.2011.02499.x

Zhou, J., Wei, Y., Yang, J., Yang, X., Jiang, Z., Chen, J., et al. (2011). Carbon budget and its response to environmental factors in young and mature poplar plantations along the middle and lower reaches of the Yangtze River, China. *Journal of Food, Agriculture and Environment*, *9*, 818–825.

Zhou, Y., Xiao, X., Zhang, G., Wagle, P., Bajgain, R., Dong, J., et al. (2017). Quantifying agricultural drought in tallgrass prairie region in the U.S. Southern Great Plains through analysis of a water-related vegetation index from MODIS images. *Agricultural and Forest Meteorology*, *246*, 111–122. https://doi.org/10.1016/j.agrformet.2017.06.007